Department of Radio Science and Engineering

The multiwavelength spectral and timing nature of the microquasar Cygnus X-3

Karri I. I. Koljonen

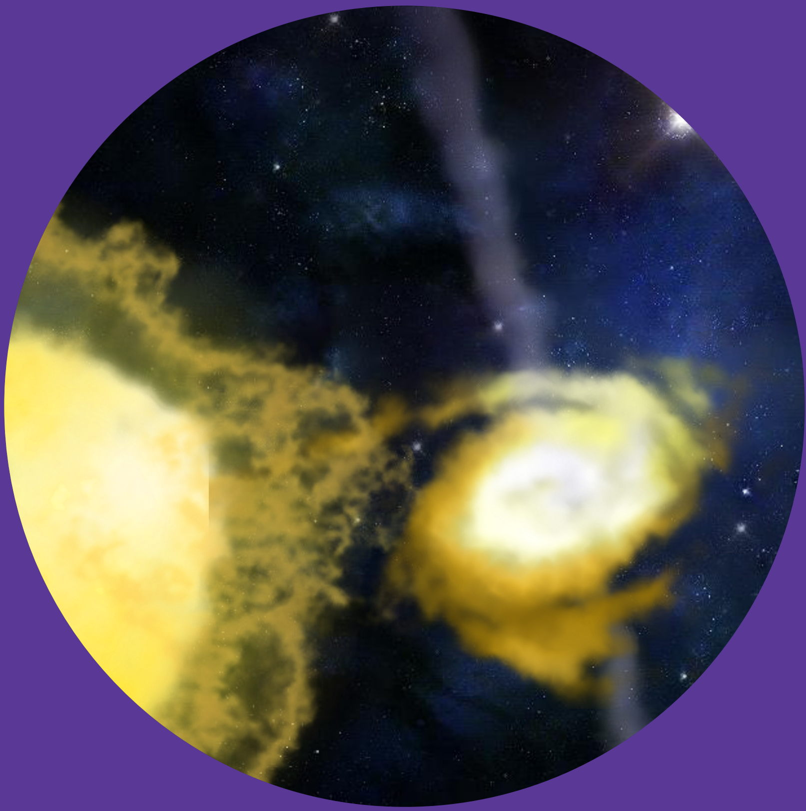

Aalto University

DOCTORAL DISSERTATIONS

Aalto University publication series
DOCTORAL DISSERTATIONS 129/2013

The multiwavelength spectral and timing nature of the microquasar Cygnus X-3

Karri I. I. Koljonen

A doctoral dissertation completed for the degree of Doctor of Philosophy to be defended, with the permission of the Aalto University School of Electrical Engineering, at a public examination held at the lecture hall S1 of the school on 27 September 2013 at 12.

Aalto University
School of Electrical Engineering
Department of Radio Science and Engineering
Metsähovi Radio Observatory

Supervising professor
Prof. Martti Hallikainen

Thesis advisors
Doc. Diana Hannikainen
Dr. Michael McCollough

Preliminary examiners
Prof. Thomas Maccarone, Texas Tech University, TX, USA
Dr. John Tomsick, University of California, Berkeley, CA, USA

Opponent
Dr. Julien Malzac, Université de Toulouse, France

Aalto University publication series
DOCTORAL DISSERTATIONS 129/2013

ISBN 978-952-60-5296-0 (printed)
ISBN 978-952-60-5297-7 (pdf)
ISSN-L 1799-4934
ISSN 1799-4934 (printed)
ISSN 1799-4942 (pdf)
http://urn.fi/URN:ISBN:978-952-60-5297-7

Unigrafia Oy
Helsinki 2013

Finland

NORDIC ECOLABEL
441 697
Printed matter

A? **Aalto University**

Aalto University, P.O. Box 11000, FI-00076 Aalto www.aalto.fi

Abstract

Author
Karri I. I. Koljonen

Name of the doctoral dissertation
The multiwavelength spectral and timing nature of the microquasar Cygnus X-3

Publisher School of Electrical Engineering

Unit Department of Radio Science and Engineering

Series Aalto University publication series DOCTORAL DISSERTATIONS 129/2013

Field of research Astrophysics

Manuscript submitted 04/03/2013 **Date of the defence** 27/09/2013

Permission to publish granted (date) 16/05/2013 **Language** English

☐ **Monograph** ☒ **Article dissertation (summary + original articles)**

Abstract

Microquasars are double star systems with a compact object, i.e. a neutron star or a black hole, accreting matter from a companion star and occasionally channeling the accreted matter into highly relativistic particle beams called jets. Amongst microquasars Cygnus X-3 is one of the most luminous and as such is an ideal source to study the connection between gravitationally heated, accreted matter close to the compact object and the jet. Cygnus X-3 is also a unique source among microquasars as it contains a massive companion star that drives a strong stellar wind, which causes additional emission scenarios when interacting with the compact object and the jet. This thesis sets out to search and study the observational phenomena caused by this special set of conditions, and attempts to resolve what the link is between different emission scenarios during violent outbursts - the birth of the jet - observed from the source.

To study the disk-jet connection in detail a hardness-intensity diagram (HID) is constructed from broadband X-ray data with simultaneous radio observations. Based on the HID a new X-ray/radio state is identified in this thesis: the hypersoft state. This state is softer in the X-ray spectra than previously classified states and exhibits very weak or nonexistent radio emission. The hypersoft state is found to be connected to the jet ejection episodes and to gamma-ray emission detected from Cygnus X-3. The fact that the sequence of events giving birth to a jet differs from other microquasars could be attributed to the strong stellar wind component and/or our line-of-sight almost coinciding with the jet axis.

In addition, quasi-periodic oscillations (QPOs) are searched for in the noise-rich X-ray lightcurves in an effort to pinpoint the environment in which these oscillations occur. The search resulted in two detections, which are associated to a certain extent with jet ejection episodes. That the QPOs coincide with outbursts points to a direct or indirect jet origin of the QPOs.

Finally, principal component analysis (PCA) is used to study the variability of X-ray emission components during outbursts. The PCA studies demonstrate a method for eliminating spectral-fit degeneracy that the X-ray community should be enticed into embracing more widely. The PCA showed that there are two main variability components in play during outbursts. In addition, a double soft-seed population Comptonization scenario is proposed that might occur in other microquasars as well, where so far mostly single soft-seed photon Comptonization models have been used. Multiple studies have shown that such a hot component is required, supporting a different source for the seed photons besides the disk.

Keywords Microquasars, Cygnus X-3, spectroscopy, time series, X-rays, radio, gamma-rays

ISBN (printed) 978-952-60-5296-0 **ISBN (pdf)** 978-952-60-5297-7

ISSN-L 1799-4934 **ISSN (printed)** 1799-4934 **ISSN (pdf)** 1799-4942

Location of publisher Helsinki **Location of printing** Helsinki **Year** 2013

Pages 179 **urn** http://urn.fi/URN:ISBN:978-952-60-5297-7

Aalto-yliopisto
Tiivistelmä
Aalto-yliopisto, PL 11000, 00076 Aalto www.aalto.fi

Tekijä
Karri I. I. Koljonen

Väitöskirjan nimi
Mikrokvasaari Cygnus X-3:n spektri- ja aikasarjaominaisuudet

Julkaisija Sähkötekniikan korkeakoulu

Yksikkö Radiotieteen ja -tekniikan laitos

Sarja Aalto University publication series DOCTORAL DISSERTATIONS 129/2013

Tutkimusala Astrofysiikka

Käsikirjoituksen pvm 04/03/2013 **Väitöspäivä** 27/09/2013

Julkaisuluvan myöntämispäivä 16/05/2013 **Kieli** Englanti

☐ **Monografia** ☒ **Yhdistelmäväitöskirja (yhteenveto-osa + erillisartikkelit)**

Tiivistelmä

Mikrokvasaarit ovat kaksoistähtiä, joissa tavallinen tähti luovuttaa ainetta tiheämmälle, neutronitähdeksi tai mustaksi aukoksi luhistuneelle tähdelle. Tiheän tähden ympärille kiertyvä aine muodostaa kertymäkiekon, jossa kitka kuumentaa ainetta niin, että se muuttuu säteilyksi. Tämän lisäksi aine voi satunnaisesti kanavoitua kompaktin kohteen läheisyydestä lähes valonnopeudella liikkuviin hiukkassuihkuihin tutkijoille vielä tuntemattoman prosessin kautta. Cygnus X-3 on yksi kirkkaimmista mikrokvasaareista. Sen kumppanitähti on raskas, voimakkaan tähtituulen omaava tähti, eikä toista vastaavaa järjestelmää vielä tunneta galaksissamme. Tässä väitöskirjassa tutkitaan ja etsitään ilmiöitä, joita ainutlaatuiset olosuhteet aiheuttavat Cygnus X-3:ssa, varsinkin kohteesta havaittujen voimakkaiden röntgen-, radio-, ja gammapurkausten aikana.

Kertymäkiekon ja hiukkassuihkujen välistä yhteyttä tutkitaan väitöskirjassa samanaikaisilla röntgen- ja radiohavainnoilla. Tulosten pohjalta Cygnus X-3:sta pystyttiin erottamaan uusi "hyperpehmeä" spektritila, jolloin kohteesta havaittu kova röntgen- ja radiosäteily on hyvin vähäistä tai olematonta. Hyperpehmeän spektritilan havaittiin olevan yhteydessä hiukkassuihku- ja gammasäteilyjaksoihin. Hiukkassuihkujen syntyminen Cygnus X-3:ssa näyttäisi tapahtuvan eri tavalla kuin muissa mikrokvasaareissa, mikä voi johtua kumppanitähden voimakkaasta tähtituulikomponentista ja/tai hiukkassuihkujen suuntautumisesta kohti Maata.

Lisäksi väitöskirjassa etsitään näennäisjaksollisia värähtelyjä kohinarikkaista röntgenvalokäyristä. Etsintä tuotti kaksi havaintoa, jotka molemmat voitiin yhdistää hiukkassuihkujaksoihin. Näennäisjaksollisten värähtelyjen samanaikaisuus purkausten kanssa viittaa vahvasti hiukkassuihkujen suoraan tai epäsuoraan osallisuuteen värähtelyjen synnyssä.

Viimeiseksi väitöskirjassa tutkitaan röntgensäteilykomponenttien vaihtelevuutta purkausten aikana pääkomponenttianalyysin avulla. Analyysin mukaan kaksi pääkomponenttia on vastuussa lähes kaikesta röntgensäteilyn vaihtelevuudesta purkausten aikana. Analyysin pohjalta ehdotettua hahmotelmaa, jossa kaksi fotonipopulaatiota Compton-siroaa hiukkassuihkuista voitaisiin soveltaa myös muiden mikrokvasaarien mallisovituksissa, joissa ylimääräinen fotonilähde on aiemmin osoitettu tarpeelliseksi. Pääkomponenttianalyysi osoittautui myös tavaksi vähentää aineiston sovittavien mallien määrää, minkä pitäisi olla houkutteleva menetelmä käytettäväksi yleisemmin röntgentähtitieteessä.

Avainsanat Mikrokvasaarit, Cygnus X-3, spektroskopia, aikasarja-analyysi, röntgen-, radio-, gammatähtitiede

ISBN (painettu) 978-952-60-5296-0 **ISBN (pdf)** 978-952-60-5297-7

ISSN-L 1799-4934 **ISSN (painettu)** 1799-4934 **ISSN (pdf)** 1799-4942

Julkaisupaikka Helsinki **Painopaikka** Helsinki **Vuosi** 2013

Sivumäärä 179 **urn** http://urn.fi/URN:ISBN:978-952-60-5297-7

Preface

It has been quite a long journey. As much as I have explored the nooks and crannies of its roads, many paths have been morphed by the people along the way (some even had a map with them). I am indebted and deeply grateful to my supervisor Diana Hannikainen after all these years of guidance, support and friendship. This work owes also much to my "across-the-pond" supervisor Michael McCollough without whom the substance of this thesis would have been a lot more thinner. This thesis, as it stands, would not have been possible without your contribution. A deep bow and a tip of the hat to you!

The research included in this thesis has been conducted in three different institutions: in the astronomy department of the University of Helsinki, in the Harvard-Smithsonian Center for Astronomy and in the Aalto University Metsähovi Radio Observatory. A huge thanks to all the people at these institutes for effortless working experience, stimulating discussions and mind-blowing ideas! Special thanks go to Osmi, Lauri, Mari, Auni, Perttu, Petri, Aleksi, Ramiro, Roberto, José, Luis, Gabor, Iouli, Alexander, Christine, Merja, Birgit, Minttu, Joni and Jonathan. A big impact to this work has been caused by the presentations and discussions with peers and colleagues in several conferences and symposia. Especially I would like to thank Robert Droulans for many fruitful discussions and collaboration! I am also deeply grateful to the 70+ collaborators that have made the research in this thesis possible. I would like to thank the pre-examiners Prof. Thomas Maccarone and Dr. John Tomsick, and the supervising professor Martti Hallikainen for their insightful comments that made this thesis much better.

While ideas are fuel for research, there is no such thing as a free lunch. I would like to acknowledge support from the astronomy department of the University of Helsinki, the Smithsonian Astrophysical Observatory, the

Academy of Finland, Jenny and Antti Wihuri foundation, Magnus Ehrnrooth foundation, the Finnish Graduate School for Astronomy and Space Physics and the Aalto University Metsähovi Radio Observatory.

I have been standing on the shoulders of giants in science as well as in life. For the latter, I would like to thank Andreas, Ville and Aapo for sharing the ups and downs of the life of a doctoral candidate. A huge thanks for lifelong support to my mother Päivi and to my uncle Osmo. Finally, a very special thanks go to my daughters Aamu and Sade, and last but not least, to my wife Kaisa for love, life and everything!

Thank you!

Helsinki, August 19, 2013,

Karri Koljonen

I have yet to see any problem, however complicated, which when you looked at it in the right way, did not become still more complicated.

—Poul Anderson

Some morning while your eating breakfast and you need something new to think about, though, you might want to ponder the fact that you see your kids across the table not as they are but as they once were, about three nanoseconds ago.

—Neil deGrasse Tyson

Getting an education was a bit like a communicable sexual disease. It made you unsuitable for a lot of jobs and then you had the urge to pass it on.

—Terry Pratchett

Contents

List of Publications

This thesis consists of an overview and of the following publications which are referred to in the text by their Roman numerals.

I **K. I. I. Koljonen**, D. C. Hannikainen, M. L. McCollough, G. G. Pooley, S. A. Trushkin. The hardness-intensity diagram of Cygnus X-3: revisiting the radio/X-ray states. *Mon. Not. R. Astron. Soc.*, 406, 307-319, March 2010.

II **K. I. I. Koljonen**, D. C. Hannikainen, M. L. McCollough. The reoccurrence of mHz QPOs in Cygnus X-3. *Mon. Not. R. Astron. Soc.*, 416, 84-88, July 2011.

III **K. I. I. Koljonen**, D. C. Hannikainen, M. L. McCollough, R. Droulans. 2006 May-July major radio flare episodes in Cygnus X-3: spectro-timing analysis of the X-ray data. *Mon. Not. R. Astron. Soc.*, 429, 1173-1188, February 2013.

IV M. Tavani, A. Bulgarelli, G. Piano, S. Sabatini, E. Striani, Y. Evangelista, A. Trois, G. Pooley, S. Trushkin, N. A. Nizhelskij, M. McCollough, **K. I. I. Koljonen**, et al. Extreme particle acceleration in the microquasar Cygnus X-3. *Nature*, 462, 620-623, December 2009.

V O. Vilhu, P. Hakala, D. C. Hannikainen, M. McCollough, **K. Koljonen**. Orbital modulation of X-ray emission lines in Cygnus X-3. *A&A*, 501, 679-686, July 2009.

VI **K. I. I. Koljonen**, D. C. Hannikainen, M. L. McCollough, G. G. Pooley, S. A. Trushkin, M. Tavani, R. Droulans. The disk/jet connection in the enigmatic microquasar Cygnus X-3. In *Proc. IAU Symp. 275, Jets at All Scales*, Buenos Aires, eds. Romero G., Sunyaev R., Belloni T., Cambridge Univ. Press, Cambridge, 24, p. 285K, February 2011.

Author's Contribution

Publication I: "The hardness-intensity diagram of Cygnus X-3: revisiting the radio/X-ray states"

The author's main responsibility was to compile the data, conduct the analyses, interpret the results, and write the paper.

Publication II: "The reoccurrence of mHz QPOs in Cygnus X-3"

The author's main responsibility was to compile the data, conduct the analyses, interpret the results, and write the paper.

Publication III: "2006 May-July major radio flare episodes in Cygnus X-3: spectro-timing analysis of the X-ray data"

The author's main responsibility was to compile the data, conduct the analyses, interpret the results, and write the paper.

Publication IV: "Extreme particle acceleration in the microquasar Cygnus X-3"

The author analyzed and discussed the X-ray data as well as the results and commented on the manuscript.

Publication V: "Orbital modulation of X-ray emission lines in Cygnus X-3"

The author provided the X-ray models used to derive the X-ray luminosities for the simulation, as well as discussed the results and commented on the manuscript.

Publication VI: "The disk/jet connection in the enigmatic microquasar Cygnus X-3"

The author's main responsibility was to compile the data, conduct the analyses, interpret the results, and write the paper.

List of Figures

List of Abbreviations

AGILE	Astro-rivelatore Gamma a Immagini Leggero
AMILA	The Arcminute Microkelvin Imager Large Array
ASM	The All-Sky Monitor
BAT	The Burst Alert Telescope
EXOSAT	European Space Agency's X-ray Observatory
FHXR	Flaring/hard X-ray
FIM	Flaring/intermediate
FSXR	Flaring/soft X-ray
FWHM	Full width at half maximum
GBI	The Green Bank Interferometer
GRID	The Gamma-Ray Imaging Detector
HEASARC	The High Energy Astrophysics Science Archive Research Center
HEXTE	The High Energy X-ray Timing Experiment
HID	Hardness-intensity diagram
HMXB	High-mass X-ray binary
HS	High/soft

IBIS	The Imager on-Board the INTEGRAL Satellite
IH	Intermediate/hard
INTEGRAL	The International Gamma-ray Astrophysics Laboratory
IS	Intermediate/soft
ISCO	Innermost stable circular orbit
ISGRI	The INTEGRAL Soft Gamma-Ray Imager
JEM-X	The Joint European X-ray Monitor
LH	Low/hard
LMXB	Low-mass X-ray binary
MHD	Magnetohydrodynamic
NASA	The National Aeronautics and Space Administration
PCA	Principal component analysis
PCU	Proportional counter unit
PDS	Power density spectrum
PICsIT	The Pixellated Imaging Caesium Iodide Telescope
QPO	Quasi-periodic oscillation
RRC	Radiative recombination continuum
RXTE	The Rossi X-ray Timing Explorer
RXTE/PCA	The Proportional Counter Array
SPI	The Spectrometer on INTEGRAL
UVOT	The UV/Optical Telescope
WR	Wolf-Rayet

XRB	X-ray binary
XRT	The X-ray telescope

List of Symbols

a	Acceleration
c	Speed of light
f	Fourier transform
g	Electron index
h	Planck constant
k	Boltzmann constant
$\dot{m}$	Accretion rate
m_e	Electron mass
m_p	Proton mass
n	Number density
$\hat{n}$	Unit vector in the direction of photon propagation
p	Pressure
q	Elementary charge
r_g	Gyroradius
s	Eigenvector
t	Time
v	Speed
$\hat{v}$	Unit vector of velocity
y	Compton y-factor

B	Magnetic field strength
B_ν	Planck function
E	Energy
F	Flux
G	Gravitational constant
I	Intensity
K	Normalization

L	Luminosity
M	Mass
$M_\odot$	Solar mass
$\mathcal{N}$	Normal distribution
P	Four-momentum
P_{comp}	Compton power
P_ν	Power density
P_{synch}	Synchrotron power
P_{tot}	Total power
Q	Quality factor
R	Radius
T	Temperature
U	Energy density
V	Volume
α	Spectral index
α_0	Pitch angle
α_i	Incident angle of photon and electron
α_f	Angle between incident electron and scattered photon
β	Velocity in the unit of the speed of the light
γ	Lorentz factor
θ	Scattering angle of photon
μ_0	Magnetic permeability
ν	Frequency
ν_g	Gyrofrequency
π	Pi
ρ	Density
σ	Stefan-Boltzmann constant
σ_T	Thomson scattering section
τ	Optical depth
Γ	Photon index

1. Introduction

Looking up in the sky with the naked eye we can marvel at the beauty of the stars and planets and the Milky Way and be forgiven for thinking of the sky as being the serene, peaceful and immutable place that humankind has imagined it to be for thousands of years before the onset of modern astronomy. But during all that time we were missing out on the real action. In deep space there are immensely dense and massive objects that can unleash gargantuan amounts of energy in a very short time. The energy radiating from these objects is such that our eyes are not able to see it, and luckily for the well-being of the inhabitants of our planet, Earth's atmosphere blocks this harmful radiation from reaching the ground. These objects are amongst the most intriguing in modern astronomy and popular culture: black holes.

Black holes are the ultimate end point in the evolution of massive stars. Following the implosion of a massive star, either by a supernova explosion, and subsequent collapse, or a full collapse of the progenitor star, the remnant can no longer withstand the gravitational pressure. What results is an extremely compact object: a black hole, from which not even light can escape. If the black hole formation occurs in a double star, or binary, system we can observe the black hole accreting matter from its companion. We cannot see the black hole directly, but in this case we are lucky to see the matter flowing into it. Therefore these black holes provide a unique laboratory for detailed studies of fundamental physics in extreme gravitational fields.

Space is literally a vast, almost empty place that is sporadically dotted with specks that we call galaxies. Even inside a relatively dense and active hub in the universe such as our own Galaxy of billions of stars, the distance between one star and the next can be measured in several light-years. This means that most of the objects outside our Solar System appear to us essentially as point-like sources, even with the greater magnifications achieved at astronomical observatories. But for astronomers even a mere point of light contains a richness of information when viewed across the whole range of radiation of the electromagnetic spectrum, to which light visible to the human eye contributes only a tiny fraction. With the appropriate instruments located on the ground, as well as in orbit around the Earth, this point of light reveals a spectrum of different energies that we observe changing with time. In the case of black holes this spectrum can be treated as a puzzle, where the individual pieces are models of the radiation processes representing the behavior of matter in extreme gravitational fields. Solving the puzzle requires fitting the pieces so that they ultimately complete the spectrum and are connected to each other consistently. The point of light is therefore transposed in our minds to an actual physical object in space, an object that can give us clues on the basic working principles of the universe like no other laboratory that is or could ever be capable of on Earth.

The subject of this thesis, a source called Cygnus X-3 – the third X-ray source to be discovered in the late 1960s in the constellation of the swan, Cygnus (Giacconi et al. 1967) – is one of the prime targets for studying the above-mentioned extreme gravitational phenomena since it is one of the most energetic X-ray emitters known to date in our Galaxy. We know that Cygnus X-3 belongs to a class of objects called microquasars, a subclass of X-ray binaries (XRBs), where the nature of the gravitational field near the black hole is so extreme that it launches huge outflows from the central regions sending electrons flying in tightly collimated jets close to the speed of light similar to their extragalactic counterparts, the quasars. However, the true nature of Cygnus X-3 remains a mystery despite extensive multiwavelength observations throughout the years.

1.1 Background

1.1.1 X-ray binaries

X-ray binaries are double star systems consisting of a compact object (essentially either a neutron star or a black hole) and usually a non-degenerate companion (i.e. any star that is fusing its hydrogen and helium reservoir). The crux to forming an XRB is the transportation of matter from the companion star to the compact object. This transportation occurs in either of two fashions: the stars orbit each other closely enough so that their gravitational potentials overlap thus allowing for the leakage of matter from the companion to the compact object or the companion's stellar wind powers an outflow of matter which is then partly captured by the compact object. The technical terms for the above methods are "Roche Lobe Overflow" and "wind accretion" respectively. The former primarily drives the low-mass X-ray binaries (LMXBs) while the latter commonly powers the high-mass X-ray binaries (HMXBs), although the opposite is by no means excluded. In both cases, due to the different rotations present in the binary (e.g. the rotation of the companion itself and the rotation of the companion around the compact object), the matter flowing toward the compact object possesses intrinsic angular momentum. Therefore, the matter does not fall directly into the compact object (or onto, for a neutron star primary) but instead starts to orbit it, and would orbit if forever if not for some mechanism that transports the angular momentum away thus causing the matter to fall ever closer to the compact object, until it eventually falls into it. The transportation of the angular momentum coupled with the rotation of the system and gravitational pull of the compact object generates a disk-like structure around the compact object referred to as an "accretion disk".

Accretion disks are observed throughout the universe around a plethora of objects from active galactic nuclei to protoplanetary systems. Apart from the other accretion disk structures in the universe, the fact that neutron stars and black holes are physically very small in size[1] allows the accretion disk in XRBs to attain very small radii and hence the matter acquires substantial gravitational energy before plunging into or onto the compact object. This energy must then be radiated away before coming to a full stop on the surface of a neutron star or, as in the case of black holes, a fraction can also be advected inside the event horizon, therefore reducing the radiation requirement. By and large, the current consensus for accretion disk angular momentum transportation is in the form of molecular viscosity and magnetic tension acting on adjacent Keplerian

[1]The radius of a neutron star is $\mathrm{R}_{\mathrm{NS}} \sim 10$ km, and the radius of a (non-rotating) black hole event horizon, often called the Schwarzschild radius, is two times the gravitational radius, $\mathrm{R}_{\mathrm{BH}} = 2\mathrm{R}_g = 2\mathrm{GM}_{\mathrm{BH}}/\mathrm{c}^2 \sim 30$ km $\mathrm{M}_{\mathrm{BH}}/(10\ \mathrm{M}_\odot)$, where G is the gravitational constant, M_{BH} the mass of the black hole, $\mathrm{M}_\odot$ the solar mass and c the speed of light. For progradely rotating black holes the event horizon decreases down to one gravitational radius for a maximally spinning black hole.

radii. In a given radius the Keplerian orbital velocity is slightly larger and slightly slower than the orbital velocities of the next radius further away and closer in from the compact object, respectively. Therefore, the adjacent fluid elements in the disk experience velocity shear which causes turbulent viscosity between the elements extracting and dissipating gravitational energy which in turn heats up the disk. The adjacent elements are also magnetically connected (the magnetic field is frozen in the disk), and the velocity shear in the disk causes the magnetic tension to increase between the elements which decreases the angular momentum of the inner and increases the angular momentum of the outer element. The accretion process turns out to be very effective at extracting gravitational energy and according to the phenomenological model of Shakura and Sunyaev (1973, in the literature it is often referred to as the α-disk model named after the turbulent viscosity that in the model is parametrized as α) the majority of the resulting thermal radiation is released at radius $R \sim$ 1–10R$_g$, and is emitted in the form of X-rays with a mean energy around 1 kiloelectronvolt (keV[2]). It is due to this radiation that we can tap into the extreme environment just outside the event horizons of black holes. The radius furthest in where a particle can have a stable orbit, and thus the furthest point where the inner edge of the accretion disk can reside is called the innermost stable circular orbit (ISCO) that has the maximum orbital velocity, ν_{ISCO} = 220 Hz (10 M$_\odot$/M$_{BH}$) for non-rotating black holes. From this we immediately see that the X-ray emission could be highly variable at the smallest timescales. It should be noted that other phenomena contribute to the X-ray variability as well, namely the orbital modulation (the companion blocking the radiation from the accretion disk) as well as the accretion states that are discussed in Section 2.2.

XRBs have been on the observing lists of astronomers from the early days of space-based X-ray instruments. Starting with the late 1940s, the sky was scanned for mere minutes at a time with Geiger counters placed inside the nozzles of sounding rockets. By the 1970s, the era of satellite missions had arrived. It was indeed the rocket missions of the 1960s that first spotted X-rays from celestial sources other than the Sun. These anomalous X-ray objects in our Galaxy were given names according to the constellations in which they were found: Scorpius X-1, Cygnus X-1, Cygnus X-2 and Cygnus X-3. To this date tens of X-ray observatories have flown and the number of XRBs has risen to about 300 sources (Liu

[2] 1 kiloelectronvolt $\sim 1.6\times10^{-16}$ Joules.

et al. 2006, 2007). One of the most influential X-ray observatories that has brought many observational constraints to accretion theories and to the inner workings of XRBs has been the *Rossi X-ray Timing Explorer* (*RXTE*). *RXTE* data has also been exhaustively used in this thesis for X-ray spectral and timing studies. After the launch of *RXTE* at the end of 1995 a plethora of X-ray observatories have been launch into space (indeed, the beginning of the millenium has been dubbed the golden-age of X-ray astronomy), among them the *International Gamma-ray Astrophysics Laboratory* (*INTEGRAL*) and *Swift* whose data is also used in this thesis.

1.1.2 Microquasars

In addition to X-ray wavelengths, XRBs have been observed at radio wavelengths. The scientific consensus is that this radiation arises from relativistic electrons circling around magnetic field lines and thus radiating synchrotron radiation. The origin of this synchrotron radiation is linked to a highly collimated outflow of plasma that has been seen emanating from extragalactic quasars. Microquasars, dubbed as such because of their similar phenomenological (and physical, albeit scaled down) appearance to extragalactic quasars, are XRBs with resolved, relativistic jets emanating from the central source, that includes the accretion disk. These jets are tightly linked to the accretion process, albeit exactly how is a very important question and is still debated among scientists. However, the prevailing view is that the jets are launched due to an interplay between a strong vertical magnetic field and the rotation of the accretion disk (Blandford and Payne 1982) and/or the black hole (Blandford and Znajek 1977), and possibly the revolving space – ergosphere – around the black hole (Punsly and Coroniti 1990) and the accretion process itself. Thus, microquasars provide ample opportunity to study the connection between the inflow of matter toward the compact object and the subsequent outflow of matter into the relativistic jets. This branch of inquiry is often referred to as the “accretion-ejection process”, or the “disk-jet connection”, and it not only applies to microquasars but also to quasars and protoplanetary systems that exhibit similar structures with accretion disks and jets. Due to their more complex structure compared to XRBs, microquasars exhibit more varied emission processes arising from the interactions and emission of the particles in the relativistic jets. The relativistic particles in the jets will orbit around the magnetic field lines producing synchrotron radiation which peaks at radio frequencies. The very same particle population can also interact with the stellar photons of the companion or with the interstellar material to produce γ-ray emission. However, the first time that this was observed from a microquasar was in Publication IV, where γ-ray emission was observed from Cygnus X-3. As seen in the above, it is crucial to obtain data simultaneously throughout the electromagnetic spectrum to understand the possible links between the different emission components and especially the disk-jet connection. About twenty microquasars are known in our Galaxy with the most studied being Cygnus X-1, GRS 1915+105, GX 339-4, SS 433 and Cygnus X-3.

1.1.3 Cygnus X-3

One of the most peculiar sources amongst microquasars is Cygnus X-3. It is known for massive outbursts that emit throughout the electromagnetic spectrum from radio to γ-rays and produce major radio flaring episodes usually with multiple flares that peak up to 20 Jy (Waltman et al. 1995), making it the single most radio luminous object in our Galaxy at its peak. It is thus a prime target for studying the emission mechanisms that arise during these violent events and probing the connection between accretion and ejection.

The most striking feature of its X-ray lightcurve (Parsignault et al. 1972) is a strong 4.8-hour periodicity which is attributed to the orbital modulation of the binary. The same periodicity has been observed in the γ-ray (Fermi LAT Collaboration et al. 2009) and in the infrared lightcurve (Mason et al. 1986). Infrared spectral observations suggest that the mass-donating companion in the binary is a high-mass Wolf-Rayet (WR) star (van Kerkwijk et al. 1992). Due to these observables Cygnus X-3 is by definition a unique source amongst HMXBs since it harbors an atypical companion star and has a very short orbital period. On the premise that the binary constitutes a WR companion and a black hole, this uniqueness has been established also through population studies (Lommen et al. 2005). Similar sources have been found in other nearby galaxies IC 10 (Prestwich et al. 2007; Silverman and Filippenko 2008) and NGC 300 (Carpano et al. 2007; Crowther et al. 2010; Binder et al. 2011), where two XRBs appear to contain WR companions and black hole primaries. These Cygnus X-3 type sources are good candidates to being the pre-stage in the evolution of binaries into a double black hole binary (Bulik et al. 2011).

The nature of the compact object is not certain, but several studies lean toward a black hole origin. Zdziarski et al. (2013) favor a low-mass black hole based on orbital kinematics measured using X-ray emission lines. Cygnus X-3 also shares spectral resemblance to other black hole XRB systems, such as GRS 1915+105 and XTE J1550−564 (see e.g. Szostek et al. 2008; Hjalmarsdotter et al. 2009) in addition to the above-mentioned extragalactic systems. Also, so far there is no evidence of a neutron star system producing such massive radio outbursts as observed from Cygnus X-3.

The distance to Cygnus X-3 is rather poorly constrained due to heavy absorption in the Galactic plane that totally obscures the optical wavelengths. Depending on the method, the distance to Cygnus X-3 is reported to be > 9.2 kpc (Dickey 1983), 8 kpc (Predehl and Schmitt 1995) and 9^{+4}_{-2} (Predehl et al. 2000, later refined to $8.4^{+0.6}_{-0.4}$ in Predehl et al. (2001)). The distance measurement of Cygnus X-3 by Ling et al. (2009) is very dependent upon the distance to the Cygnus OB2 association, but they give a conservative range of 6–10 kpc. Thus, we adopt 9 kpc as the distance to Cygnus X-3 in this thesis as it overlaps nearly all of the measurements.

The X-ray spectral and timing properties of Cygnus X-3 show a disparity contributing to the difficulty of interpreting the nature of the system. Apart from the strong X-ray modulation, the X-ray variability of Cygnus X-3 is otherwise very nondescript and does not show any resemblance to other XRBs. On the other hand, the X-ray spectra of Cygnus X-3 are notoriously complex and more or less resemble the X-ray spectra observed in other XRBs but differ somewhat in certain features and in the type of spectra. This disparity could be explained by the interaction of the strong stellar wind of the WR companion with the compact object as suggested in Fender et al. (1999) and Szostek and Zdziarski (2008) if the accretion disk is enshrouded partially or wholly in the stellar wind.

1.2 Objective and scope

The approach for studying Cygnus X-3 is two-fold in this thesis: spectral information is obtained through multiwavelength observations from radio to γ-ray wavelengths and timing information is obtained through high time-resolution X-ray observations. The methods are complementary to each other and help us to understand the nature of this system, and subsequently provide us with more insight into the class of radio-jet XRBs as a whole. The research topics of this thesis are introduced below.

Topic 1: Using simultaneous X-ray and radio observations to study the disk-jet connection in Cygnus X-3.
The classification of the different spectral states of Cygnus X-3 has progressed on two fronts: radio (Waltman et al. 1996; McCollough et al. 1999) and X-rays (Szostek and Zdziarski 2008; Hjalmarsdotter et al. 2009). However, due to the link between accretion (producing the X-ray emission) and ejection (producing the radio emission) in microquasars, it seems natural to look for mutual and thus simultaneous behavior in both emission regimes. The first step in this direction was undertaken by Szostek et al. (2008) where X-ray and radio monitoring observations were examined together. However, the monitoring frequencies gave only a rough estimate of the underlying broadband X-ray energy spectral distribution and thus a better description of the disk-jet connection might be revealed through a more detailed study. Publication I and Publication VI deal with this subject by utilizing simultaneous radio monitoring with broadband X-ray spectra. The inclusion of a third wavelength regime, γ-rays, is introduced in Publication IV to shed more light onto the disk-jet connection and the energetics of the jet.

Topic 2: Searching for low-frequency quasi-periodic oscillations and their link to a special set of conditions in Cygnus X-3.
The X-ray timing properties of Cygnus X-3 are remarkably nondescript apart from the strong orbital modulation. High-frequency timing phenomena, such as quasi-periodic oscillations (QPOs) that are used to study the strong gravitational regime of XRBs/microquasars, are most likely washed out by scattering in Cygnus X-3. In addition, the most prominent noise component is caused by red noise. There is tendency for the eye to identify low-frequency peaks in the power density spectrum (PDS), thus requiring careful analysis of possible low-frequency signals. However, there are indications that there might be an increase of variability in the form of low-frequency QPOs in the mHz regime (van der Klis and Jansen 1985). As these QPOs seem to be fleeting and sporadic events, they most likely are caused by a special set of conditions in the system. The possible special set of conditions was searched for in Publication II and Publication VI with the aid of radio monitoring and millisecond X-ray lightcurves.

Topic 3: Searching for the interplay of the compact object

with the stellar wind in Cygnus X-3.
Cygnus X-3 displays unique properties in the X-ray spectra when compared to other XRBs/microquasars. There are hints that these peculiarities are linked to the interplay between the compact object and the dense stellar wind emanating from the companion WR star (Szostek and Zdziarski 2008). Publication III and Publication V concentrate on the search for and the study of the effects caused by the stellar wind on the X-ray spectra of Cygnus X-3 using a novel spectro-timing analysis method in the former and high-resolution X-ray spectroscopy in the latter.

1.3 Dissertation structure

The overview of this thesis continues with a more detailed introduction to radiation mechanisms, X-ray states and relativistic jets in Chapter 2. The observations and analysis methods used in this thesis are presented in Chapter 3. The results are presented in Chapter 4 and discussed in Chapter 5.

2. Theoretical foundation

2.1 Radiation mechanisms

Occasionally dubbed the “fifth form of matter”, plasma is the most important medium in the astrophysical context. The unique characteristics of quasi-neutrality and the large mass difference between electrons and protons give rise to a plentitude of interactions between the electrons and photons, as well as between electrons and magnetic fields. The most important radiation processes when studying microquasars and XRBs are Compton scattering, synchrotron radiation, thermal disk radiation and line emission, which are briefly described in the following. A full treatment of these processes can be found e.g. in Rybicki and Lightman (1979) or Longair (2011).

2.1.1 Compton scattering

One of the most important interactions between electrons and photons in astrophysical plasmas is Compton scattering (Fig. 2.1). In a scattering event an incident photon with four-momentum $P_{\gamma i} = (E_i/c)(1, \hat{n}_i)$, where E is the energy and $\hat{n}$ is the unit vector in the direction of propagation of the photon, hits an incident electron moving at arbitrary speed with four-momentum $P_{ei} = \gamma_i m_e(c, \hat{v}_i)$, where $\gamma = (1-\beta^2)^{-1/2} = (1-v^2/c^2)^{-1/2}$ is the Lorentz factor, m_e is the mass and $\hat{v}$ is the unit vector of velocity of the electron. This interaction results in an energy exchange for the photon and electron leaving the scattering site with four-momenta $P_{\gamma f} = (E_f/c)(1, \hat{n}_f)$ and $P_{ef} = \gamma_f m_e(c, \hat{v_f})$, respectively. Energy-momentum conservation states that $P_{\gamma i}+P_{ei} = P_{\gamma f}+P_{ef}$ which can be written as $P_{\gamma f}\cdot P_{\gamma i}+P_{\gamma f}\cdot P_{ei} = P_{\gamma f}\cdot P_{ef}$. It can be shown using Lorentz invariants ($P_{\gamma\mu}P^{\gamma\mu} = 0$, $P_{e\mu}P^{e\mu} = -m_e^2c^2$ and $(P_{\gamma i} + P_{ei})_\mu(P_{\gamma i} + P_{ei})^\mu = (P_{\gamma f} + P_{ef})_\mu(P_{\gamma f} + P_{ef})^\mu$)

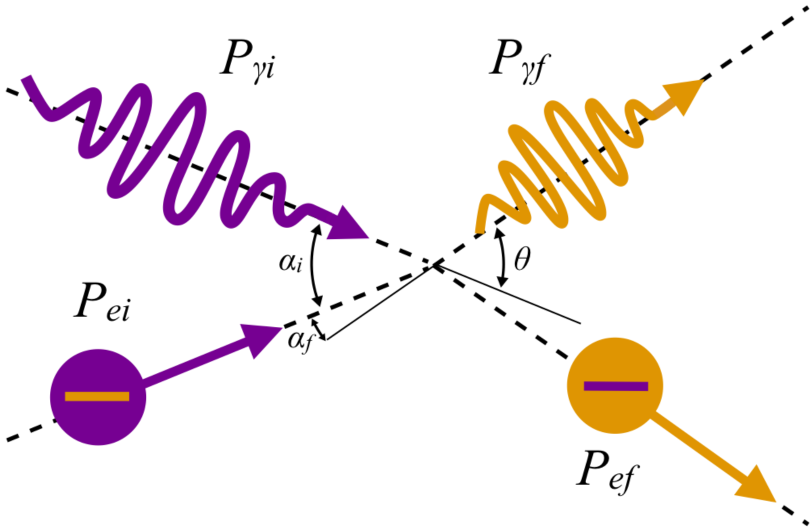

Figure 2.1. The geometry of Compton scattering.

that $P_{\gamma f} \cdot P_{ef} = P_{\gamma i} \cdot P_{ei}$, thus we get $P_{\gamma f} \cdot P_{\gamma i} + P_{\gamma f} \cdot P_{ei} = P_{\gamma i} \cdot P_{ei}$. Inserting the four-momenta in vector notation and solving the above gives for the change in photon energy

$$\frac{E_f}{E_i} = \frac{1 - \beta_i \cos \alpha_i}{1 - \beta_i \cos \alpha_f + \frac{E_i}{\gamma_i m_e c^2}(1 - \cos \theta)}, \tag{2.1}$$

where the angles are defined as $\cos \theta = \hat{n}_i \cdot \hat{n}_f$ (the scattering angle), $v_i \cos \alpha_f = \hat{n}_f \cdot v_i$ and $v_i \cos \alpha_i = \hat{n}_i \cdot v_i$. In the electron rest frame ($\beta_i = 0, \gamma_i = 1$) the incoming radiation is symmetric, thus the average change in energy for a photon is $E_f = (1 + E_i/m_e c^2)^{-1}$, where we see that $E_f < E_i$ and energy is lost to the electron recoil. However, in astrophysical plasmas the electrons are normally highly relativistic ($\beta_i \to 1, \gamma_i \gg 1$). In this case the photons can acquire vast amounts of energy and this process is referred to as "inverse Compton scattering". Qualitatively, the incoming radiation is symmetric but the outgoing Comptonized radiation is highly beamed in the direction of the electron velocity ($\cos \alpha_f \approx 1, \langle \cos \alpha_i \rangle = 0$), thus we get $E_f/E_i \approx 1/(1-\beta_i) = 2\gamma_i^2$. Therefore, the photon has gained energy that is many times its initial energy. For example, with large Lorentz factors (e.g. $\gamma = 10^3$) 1 GHz radio emission is boosted to 1 PHz emission, corresponding to the ultraviolet portion of the electromagnetic spectrum; or optical emission ($\nu \sim 10^{14}$ Hz) gets boosted to γ-rays ($\nu \sim 10^{20}$ Hz). Of course, energy conservation states that the maximal energy gained by the photon is $E_{\max} = \gamma m_e c^2$ corresponding to the full electron energy.

In a low optical depth regime the Compton power is given as

$$P_{\text{comp}} = \frac{dE_{\text{rad}}}{dt} = \frac{4}{3}\sigma_T c\gamma^2\beta^2 U_{\text{rad}}, \tag{2.2}$$

where σ_T is the Thomson scattering section and U_{rad} is the initial radiation energy density. From the above the total Compton power per unit volume from a medium of relativistic electrons can be calculated provided that the velocity distribution of electrons is known. Usually, the distribution of electrons is thermal, non-thermal or a mixture of both. For a non-relativistic, thermal distribution of electrons $\langle\beta^2\rangle = 3kT_e/m_ec^2$, where k is the Boltzmann constant T_e is the temperature of the electrons, and $\gamma \approx 1$ we get

$$P_{\text{tot}} = \left.\frac{dP_{\text{comp}}}{dV}\right|_{\text{thermal}} = \frac{d^2E_{\text{rad}}}{dtdV} = \frac{dU_{\text{rad}}}{dt} = 4\sigma_T cU_{\text{rad}} n_e\left(\frac{kT_e}{m_ec^2}\right), \tag{2.3}$$

where n_e is the total number density of electrons. In the case of non-thermal ($\gamma \gg 1, \beta \approx 1$) power law electron distribution, where $n_e = \int K\gamma^{-g}d\gamma$, K is the normalization of the distribution and γ ranges from γ_{min} to γ_{max} the total Compton power is

$$P_{\text{tot}} = \int P_{\text{comp}} n_e(\gamma)d\gamma = \frac{4}{3}\sigma_T cU_{\text{rad}}\frac{K}{3-g}(\gamma_{\text{max}}^{3-g} - \gamma_{\text{min}}^{3-g}). \tag{2.4}$$

Qualitatively, the resulting energy spectrum in the power law case (recalling $E_f \propto \gamma^2 E_i$ from above) is

$$\frac{d^2E_{\text{rad}}}{dtdVdE_f} = \frac{d\gamma}{dE_f}\frac{d^2E_{\text{rad}}}{dtdVd\gamma} \propto \frac{1}{\gamma}\gamma^{2-g} = \gamma^{1-g} \propto E_f^{(1-g)/2}. \tag{2.5}$$

Thus, the scattered energy spectrum is a power law but with a spectral index $\alpha = (g-1)/2$ and a photon index $\Gamma = (g+1)/2$.

In the discussion so far we have considered only a single scattering event. However, several scattering events can take place depending on the electron scattering optical depth $\tau_{es} \approx n_e\sigma_T R$, where R is the size of the scattering region in question. For multiple scattering events inverse Compton scattering is characterized by a Compton y-factor, which is defined as the average fractional energy gained per scattering by the photons multiplied by the mean number of scattering events. The mean number of scattering events is obtained from the optical depth τ_{es}, where a value of $\tau_{es} \sim 1$ means that on average, a photon will scatter once before escaping the region. Specifically, the mean number of scattering events is approximately $\max(\tau_{es}, \tau_{es}^2)$ and in the case of non-relativistic, thermal Comptonization the fractional energy per scattering is $dU_{\text{rad}}/U_{\text{rad}} = (4kT_e/m_ec^2)d\tau_{es}$. Thus, the y-factor is defined as

$$y \equiv \frac{4kT_e}{m_ec^2}\max(\tau_{\text{es}}, \tau_{\text{es}}^2). \tag{2.6}$$

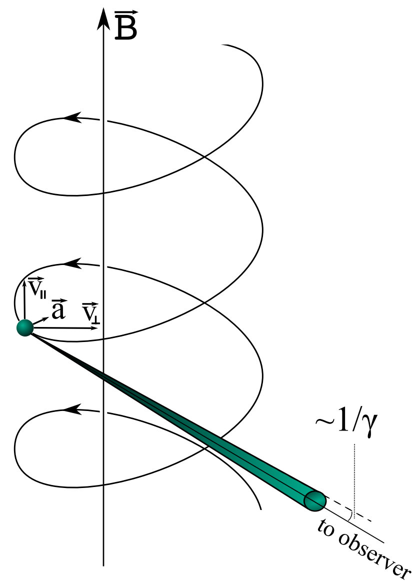

Figure 2.2. The mechanism for producing synchrotron radiation. A charged particle spiraling around a magnetic field line is accelerated and emits radiation into a tight radiation cone.

The slope of the scattered radiation energy spectrum is characterized by the y-factor so that when $y \ll 1$ there is negligible change in the energy spectrum, whereas $y \sim 1$ is governed by the Kompaneets equation and describes a power law energy spectrum with an exponential cut-off. In this case the power law portion of the energy spectrum has a slope $\alpha = -(3/2) \pm \sqrt{(9/4) + (4/y)}$ (Rybicki and Lightman 1979), where the '$+$' correspond to the up-scattered and the '$-$' correspond to the down-scattered photons. Thus, it is possible to obtain a scattered power law spectrum, even if the scattering electrons have a thermal distribution. The values $y \gg 1$ are called saturated Comptonization where the incident photon spectrum approaches the distribution of the scattering electrons, i.e. the electrons and photons will come into thermal equilibrium where the scattered photon spectrum will peak at $E \simeq 2.8kT_e$.

2.1.2 Synchrotron radiation

Synchrotron radiation arises from the relativistic motion of charged particles in a magnetic field, and thus is a prominent radiation component in astrophysical plasmas since strong magnetic fields are present in many astrophysical sources. The origin of this radiation is usually due to electrons moving at relativistic speeds, since they are lighter than protons and hence more easily accelerated. The non-relativistic case is referred to as "cyclotron radiation". The motion of electrons in the presence of a magnetic field consists of a constant velocity component along a magnetic field line and circular motion around it, i.e. a spiral path with a constant pitch angle (Fig. 2.2). The radius is usually referred to as the "gyroradius" (r_g) of the electron and its corresponding frequency the "gyrofrequency":

$$\nu_g = \frac{(\beta_\perp / r_g)}{2\pi} = \frac{qB}{2\pi\gamma m_e}, \tag{2.7}$$

where B is the magnetic field strength and q is the elementary charge. Thus, the parallel and perpendicular components of acceleration to the direction of magnetic field are ($a_\parallel = 0$) and $a_\perp = \nu_g \beta_\perp$, respectively. The total emitted power of the particle can be obtained via the relativistic Larmor formula: $(\mu_0 q^2/6\pi c)\gamma^4(\gamma^2 a_\parallel^2 + a_\perp^2)$, where μ_0 is the magnetic permeability of free space. Inserting $a_\perp$ and integrating over all pitch angles ($\langle \sin^2 \alpha_0 \rangle = 2/3$) for a given velocity β gives for the synchrotron power:

$$P_{\text{synch}} = \frac{2}{3}\frac{\mu_0}{6\pi c}\frac{q^4}{m^2}\gamma^2\beta^2 B^2. \tag{2.8}$$

A more familiar form is achieved when the above equation is expressed in terms of the Thomson cross-section $\sigma_T = \mu_0^2 q^4/6\pi m^2 c^2$ and magnetic energy density $U_B = B^2/2\mu_0$:

$$P_{\text{synch}} = \frac{4}{3}\sigma_T c \gamma^2 \beta^2 U_B, \tag{2.9}$$

which is exactly the same as for Compton scattering power with the change of the radiation energy density U_{rad} to magnetic energy density U_B. Synchrotron radiation can be thought to arise from Compton scattering off of virtual photons of the magnetic field. Thus, an important relation in the astrophysics is

$$\frac{P_{\text{comp}}}{P_{\text{synch}}} = \frac{U_{\text{rad}}}{U_B}, \tag{2.10}$$

which provides a self-regulating mechanism for a synchrotron-emitting plasma: high-energy electrons produce photons that in turn get inverse Compton scattered by the very same electrons, thus removing energy, or cooling, the electrons. In the literature this interplay is known as the synchrotron self-Compton mechanism. If the radiation energy density is greater than the magnetic energy density in the beginning, this mechanism eventually extracts all the available energy from the electrons and shuts down the synchrotron emission. Also, similar to Compton scattering, the photon spectrum arising from the synchrotron emission of electrons with a power law distribution is a power law with a spectral index of

$\alpha = (g-1)/2$, where the g is the original index of the electron distribution. At low frequencies the optical depth for the synchrotron photons increases and they are unable to escape the region, producing a low energy cut-off at $\nu \propto \gamma^2$ and a spectrum that follows a power law with a spectral index of $-5/2$.

2.1.3 Thermal disk radiation

In order to cool the relativistic electrons via Compton scattering a population of soft photons is needed. One possible source of soft photons is the above-mentioned synchrotron radiation, but in the case of microquasars soft photons can also arise from blackbody radiation of thermal plasma in the accretion disk and from bremsstrahlung radiation, i.e. the radiation emitted by electrons when accelerated by the Coulomb field of another charged particle, although the latter is usually considered to be a negligible radiation process in microquasars. However, it might play a role in the spectral energy distribution of Cygnus X-3 as discussed in Publication III.

If the radiation field has uniform temperature it emits a characteristic blackbody spectrum, whose intensity is given by the Planck function:

$$B_\nu = \frac{2h\nu^3}{c^2}\frac{1}{e^{h\nu/kT}-1}, \tag{2.11}$$

where h is the Planck constant. Integrating over all frequencies reduces the above equation to $B = (\sigma/\pi)T^4$, where σ is the Stefan-Boltzmann constant, thus the radiation of a blackbody emitter is governed by its temperature alone. In the accretion disk the temperature of the plasma is governed by the distance from the central source. For an accretion rate $\dot{m}$ the kinetic energy gained from the gravitational potential is turned into heat at a rate $(1/2)\dot{m}v^2$, which gives the accretion luminosity for the non-relativistic case:

$$L = \frac{1}{2}\frac{1}{2}\dot{m}v^2 = \frac{GM\dot{m}}{2R} = \frac{1}{2}\dot{m}c^2\frac{R_g}{2R}, \tag{2.12}$$

where the first half comes from the virial theorem that states that only half of the gravitational potential energy can be radiated. Eq. 2.12 shows that for constant accretion rate the luminosity of the disk is inversely proportional to the distance (i.e. $L \propto R^{-1}$). On the other hand, if this luminosity is produced by blackbody radiation the luminosity is proportional to the temperature (i.e. $B \propto T^4 \Rightarrow L \propto R^2T^4$). Thus, the temperature profile of the disk is proportional to the radius as $T(R) \propto R^{(-3/4)}$. A full analysis

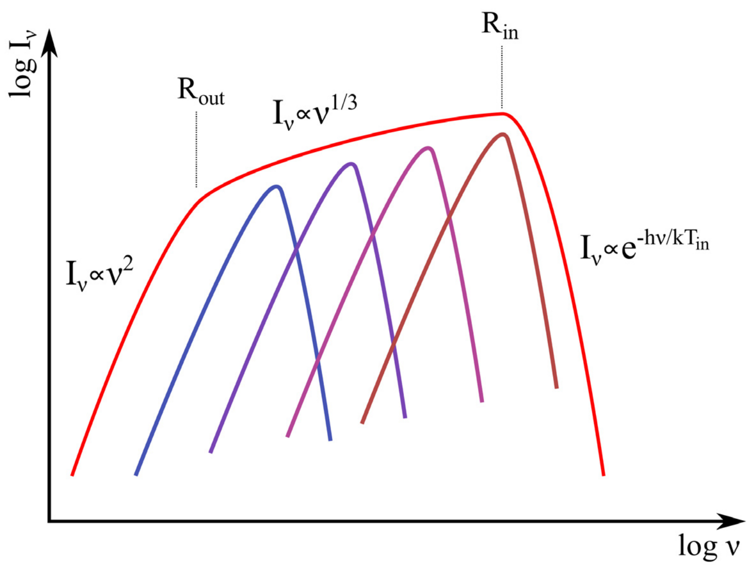

Figure 2.3. The spectrum from a classical accretion disk where black body radiation from different annuli ranging from the ISCO (R_{in}) to the disk outer radius (R_{out}) is summed up to form a multi-color accretion disk model.

gives for the temperature profile for the non-relativistic case (Shakura & Sunyaev, 1973):

$$T(R) = \left(\frac{3GM\dot{m}}{8\pi\sigma R^3} \left[1 - \left(1 - \frac{R_{in}}{R} \right)^{1/2} \right] \right)^{1/4}. \tag{2.13}$$

This is usually referred to as the "classical" disk, or optically thick, geometrically thin disk and it is used in this thesis as the model for the accretion disk emission. However, many problems remain in modeling the accretion disk accurately. To name a few, the inclusion of metallicities in the plasma and the advection of matter through the event horizon of a black hole will modify the emission spectrum. For high luminosities the thin disk approximation breaks down and a lot of effort has been made to study optically thin and geometrically thick disks. In particular, the high luminosity of the plasma near the compact object can drive a large wind off the outer portion of the disk, thus varying the $\dot{m}$ which was considered a constant in the classical solution. However, observations are inconclusive as to which solution is operating and when.

The energy spectrum, or intensity, of the classical disk (Fig. 2.3) can be obtained by inserting Eq. 2.13 into Eq. 2.11 and integrating over the whole disk from its inner edge R_{in} to the outer edge R_{out}:

$$I_\nu \propto \int_{R_{in}}^{R_{out}} 2\pi R B_\nu[T(R)] dR. \tag{2.14}$$

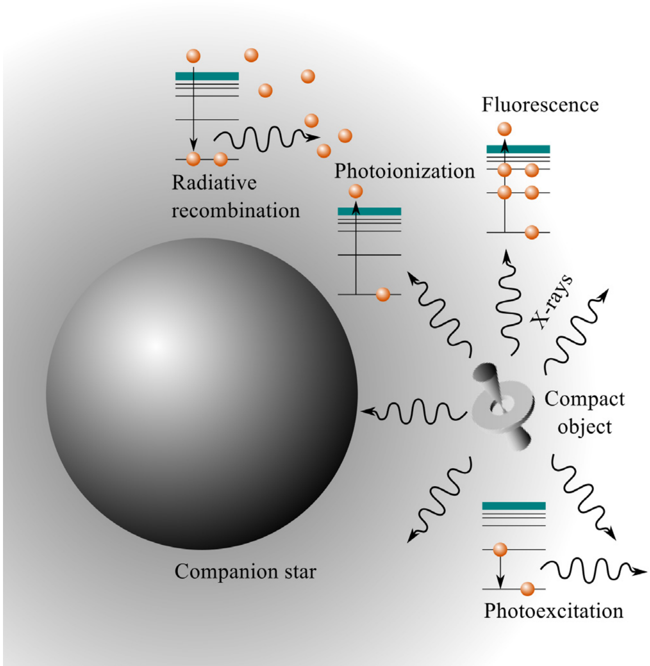

Figure 2.4. Line-forming processes in the stellar wind near the ionizing X-ray radiation of the compact object.

Using the relation $T \propto R^{-3/4}$ and changing the variables appropriately to $dR \propto (1/T)^{1/3} d(1/T)$ this changes to:

$$I_\nu \propto \int_{1/T_{in}}^{1/T_{out}} \left(\frac{1}{T}\right)^{4/3} \nu^3 \frac{1}{e^{h\nu/kT}-1} \left(\frac{1}{T}\right)^{1/3} d\left(\frac{1}{T}\right). \tag{2.15}$$

Simplifying this by using a variable $x = h\nu/kT$ gives:

$$I_\nu \propto \frac{\nu^3}{\nu^{8/3}} \int_{h\nu/T_{in}}^{h\nu/T_{out}} x^{5/3} \frac{1}{e^x - 1} dx. \tag{2.16}$$

In the middle of the spectrum we can approximate the limits as $h\nu/T_{in} \ll 1 \sim 0$ and $h\nu/T^{out} \gg 1 \sim \infty$, which reduces the integral to a constant value. Thus, the spectrum goes as $I_\nu \propto \nu^{1/3}$ in the frequency range corresponding to a range in annuli between R_{in} and R_{out}. The frequencies below $\nu = kT_{out}/h$ are in the Rayleigh-Jeans portion of the spectrum and thus $I_\nu \propto \nu^2$. Respectively, the frequencies above $\nu = kT_{in}/h$ are in the Wien portion of the spectrum and thus $I_\nu \propto \exp(-h\nu/kT_{in})$.

2.1.4 Continuum modifiers

On top of the continuum produced by the processes described above the final spectrum received by the detector gets modified by absorption and subsequent line emission (see Fig. 2.4 for a collection of line-forming processes). Especially in HMXBs, such as Cygnus X-3, the massive stellar wind emanating from the companion star brings matter into the vicinity of the intense radiation field of the compact object. In the X-ray band one of the cooling processes through which photons lose energy to the surrounding matter is photoionization. In this process an incident photon hits an ion or an atom and ejects an electron whose binding energy is less than the energy of the photon. The energy levels equivalent to the binding energy for the electrons inside atoms are called absorption edges, as photons with higher energy than the binding energy will be absorbed by these atoms. This process produces a sharp edge in the energy spectrum that reduces the number of photons received above the binding energy and scales roughly as E^{-3}. The inverse process of photoionization where an ion captures an electron is called radiative recombination. As the captured electron energies are distributed continuously the resulting emission from radiative recombination forms a continuum (radiative recombination continuum or RRC). As this process is dependent on the characteristics of the electron population it can be used as a diagnostic tool of the plasma. The RRCs can be found in the energy spectrum above the recombination edge with a width that is approximately the same as the temperature of the electrons kT_e. The ions can capture the electrons to any free energy level, and if it is not the ground state it leaves the ions in an excited state, followed by the subsequent decay of the excited state to the ground state releasing spontaneous emission. This emission generates photons that will contribute to the emission line of the ions in the plasma. Another process contributing to the emission (and absorption) line formation is photoexcitation, where a photon excites a bound state of an ion resulting in emission when the excited electron decays back to the original energy level.

Another important process for line emission from XRBs is fluorescence, where an inner-shell electron of ions in a low charge state (i.e. “cold” ions) are photoionized leaving the ions in an excited state. This is followed by the filling of the hole of the ejected electron with an electron from higher energy levels which produces a photon. Alternatively, this energy can be transferred to another electron, called an Auger electron, which is then ejected from the ion. Perhaps the single, most important emission line in XRBs is the fluorescence Kα emission line for neutral iron at 6.4 keV, which is produced close to the compact object and can be used to study

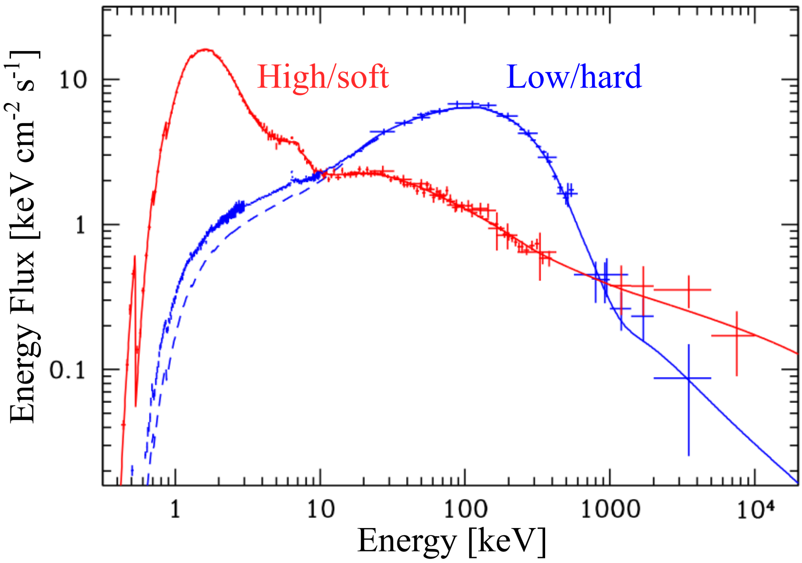

Figure 2.5. Canonical X-ray states from Cyg X-1 (low/hard state: blue, high/soft state: red). Modified from McConnell et al. (2002)

the plasma in the vicinity of the strong gravitational field of the compact object.

In addition to the modifications to the energy spectrum close to the compact object the radiation gets modified by the interstellar matter along the line-of-sight that produces an extra absorption factor spanning from the infrared to the soft X-rays.

2.2 X-ray states

Soon after the discovery of XRBs they were found to be highly variable in the X-ray band from 1 to 10 keV (Tananbaum et al. 1972), varying from a low luminosity state to a high luminosity state. Often these states are referred to as "the low state" and "the high state" (e.g. van der Klis 1994; Nowak 1995; McClintock and Remillard 2006). However, one has to bear in mind that these labels were assigned in order to explain the source behavior in this relatively narrow band. If a wider bandwidth is taken into account it is possible that the low state is more luminous, i.e. the bolometric luminosity of the source is greater in the low state than the bolometric luminosity in the high state. As mentioned in Section 1.1.1 the α-disk model was established to explain the blackbody-like high state spectra. In the high state the accretion disk dominates the geometry of the system with little or no hot corona, and most of the bolometric luminosity is concentrated on photon energies below 10 keV resulting in a "soft" spectrum. However, the low state is dominated by a power law-like component which extends beyond 10 keV (a weaker high energy tail is seen in the high state as well). This component is taken to represent the inverse Comptonization of soft seed photons in a plasma cloud of hot electrons. These hot electrons can often be located in multiple places as described below. Thus, they are often dubbed just as "the corona", a term which embodies all the different possibilities for the origin of the hot electrons. In the low state the coronal component in the source dominates, and the disk is either greatly reduced or then immersed inside the corona resulting in a "hard" spectrum where the bolometric luminosity is concentrated on photon energies above 10 keV. This spectral bimodality has been added to the state vocabulary so that the high state becomes the high/soft (HS) state and the low state the low/hard (LH) state. These states will be referred to as the canonical X-ray states of XRBs in this thesis (see Fig. 2.5). In the "intermediate" states, when the source is transiting from the HS state to the LH state or vice versa, we see the influence of both components (disk and corona) to differing extents.

The common view is that there is a change in the rate at which matter flows ($\dot{m}$) from the companion star to the accretion disk that ultimately drives the spectral evolution. An important limit is set when considering the radiation pressure gradient from the intense X-ray radiation near the ISCO and the gravitational pressure gradient of the inflowing matter. The limit where the radiation pressure gradient becomes equal to the gravitational pressure gradient, therefore stalling the accretion of matter toward the compact object, is called the Eddington luminosity or Eddington limit, and it was originally derived for stars (spherically symmetric objects), but it can be used to approximate the behavior of accretion disks as well. Equating these two pressure gradients yields:

$$\frac{dp}{dR} = -\frac{GM(R)\rho(R)}{R^2}. \tag{2.17}$$

When taking into account only the Thomson scattering of photons from the electrons of the inflow the radiation pressure gradient is proportional to the luminosity L of the disk so that

$$\frac{dp}{dR} = -\frac{\sigma_T \rho L}{4\pi R^2 m_p c}. \tag{2.18}$$

Inserting this into Eq. 2.17 gives the Eddington luminosity:

$$L_{Edd} = \frac{4\pi G M m_p c}{\sigma_T} \simeq 1.3 \times 10^{38} \frac{M}{M_\odot} \mathrm{erg/s}. \qquad (2.19)$$

When the accretion rate is high (close to the Eddington luminosity) the material in the accretion disk pushes close to the ISCO and radiates predominantly thermal, blackbody radiation driving the system into the HS state by cooling the hot electrons via Coulomb collisions and Compton scattering. On the other hand, when the accretion rate is low the inflow toward the compact object is much reduced and the Coulomb coupling between protons and electrons is weak. This in turn leads to diminished radiation and drives the system into the LH state, as most of the heat is contained in protons, which do not radiate, and energy transfer to the electrons is inefficient. The hot flow is then cooled by advecting the matter into the black hole, thus the designation of this scenario: advection-dominated accretion flow (Ichimaru 1977; Narayan and Yi 1994). There is still an ongoing debate as to whether the accretion disk is truncated away from the ISCO (e.g. Tomsick et al. 2009) or if the accretion disk radiation close to the ISCO is just highly diminished (Reis et al. 2009). Another scenario favored for producing the high energy tail in the HS state is usually attributed to active regions above the disk that are caused by small patches of energetic electrons energized by a magnetic reconnection of the magnetic field lines of the accretion disk. Since microquasars contain relativistic and thus Comptonizing electrons in the jet, it can also be added to the list of possible locations for Comptonizing the disk photons. Therefore, the radio emission – indicating the presence of the jet – is also an important measure of the state classification. This is particularly important for strong radio sources like Cyg X-3 as will be described in Section 2.3.1.

In addition to the canonical states XRBs exhibit various transition or intermediate states in between the HS and LH states. These intermediate states are by virtue much more rare and transitionary but they convey important information on the relationship between the two canonical spectral components in XRBs. One of the most widely used tools of the trade for studying the spectral evolution and intermediate states is a hardness-intensity diagram (HID, described in more detail in Section 3.2.1), which shows the X-ray intensity (i.e. source luminosity not corrected for distance) as a function of hardness ratio (a ratio between the intensities of two spectral bands, usually one for soft X-rays with intensities below 10 keV and one for hard X-rays with intensities above 10 keV). In spite of the fact that XRB X-ray lightcurves are highly variable, the hardness ratio is much more stable and usually exhibits smoother changes and it is therefore a good proxy of the accretion state of the system.

2.2.1 X-ray spectral states of Cygnus X-3

Cygnus X-3 displays multiple X-ray states, including not only the canonical HS and LH states but also three (Szostek et al. 2004) or four (Publication I) other states in between (see Figure 2.6). The classification of these states is defined by their spectral hardness and the strength of the soft, disk-like component of the spectra. The first successful physical interpretation of the broadband X-ray spectrum (Vilhu et al. 2003) consisted of a thermal Comptonization component and Compton reflection from an ionized medium with parameters similar to those found for black hole binaries at high Eddington rates, with the exception of very strong absorption. Ever since, all the broadband X-ray spectra from all the spectral states of Cygnus X-3 have been fitted with a model where the main spectral component is thermal/non-thermal Comptonization (Hjalmarsdotter et al. 2009, Publication I). Thus, it appears that Cygnus X-3 is Comptonization dominated. The peculiar cut-off at ~ 30 keV in the harder spectra, which is not observed in any other XRBs, can be explained by Compton downscattering of high energy photons by relatively cooler electrons that are part of the plasma cloud surrounding the compact object (Zdziarski et al. 2010). This plasma cloud could form as the result of an interaction between the compact object and the stellar wind from the WR companion. The interaction of the Comptonized photons with the stellar wind is evident in the form of strong emission lines, particularly iron lines, that are formed through photoionization. Thus, the unique environment of Cygnus X-3 produces unique spectral features.

2.2.2 X-ray timing properties of Cygnus X-3

The PDS of Cygnus X-3 was studied in Willingale et al. (1985) and was found to be well described by a power law of index $\alpha = 1.8$ in the frequency range 10^{-5}–0.1 Hz. This result has been more or less verified in further studies by Choudhury et al. (2004, $\alpha \sim 1.5$), Axelsson et al. (2009, $\alpha \sim 2$ in the canonical HS state and $\alpha \sim 1.8$ in the LH state). van der Klis and Jansen (1985) found short intervals (5–40 cycles) of mHz quasi-periodic features in the PDS during the HS state and possibly also during the LH

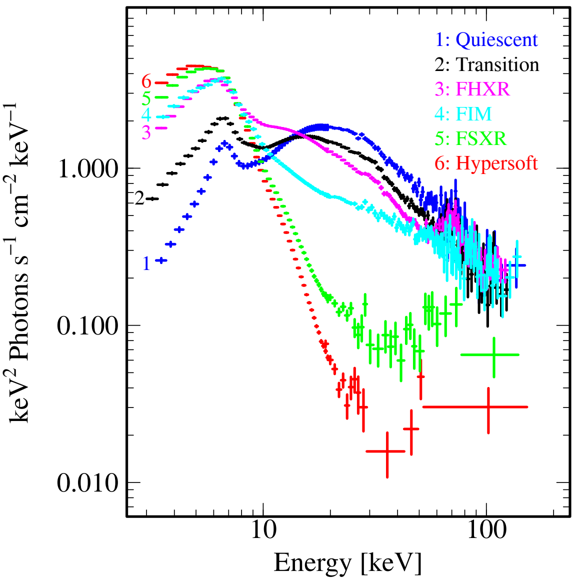

Figure 2.6. X-ray spectral states of Cygnus X-3. The spectra are colored and labeled with different colors and numbers according to the legend. The state nomenclature follows the one defined in Publication I, where the quiescent and transition states correspond to the LH X-ray state with moderate radio emission, the flaring/hard X-ray (FHXR), the flaring/intermediate (FIM) and the flaring/soft X-ray (FSXR) states correspond to the intermediate X-ray states with radio flaring, and the hypersoft state corresponds to the HS state with quenched radio emission.

state using data from the European Space Agency's X-ray Observatory (*EXOSAT*). A mHz feature in the Cygnus X-3 hard X-ray lightcurve was also found in a balloon flight study by Rao et al. (1991). On the contrary, no QPOs were found in the *RXTE* study in Axelsson et al. (2009) in either the HS or LH states of the source. The discrepancies between the reported results clearly show that these transient features are short-lived and sporadic or time-sensitive events. In addition, no strict method of calculating the significance of the peaks in the PDS was undertaken in the previous studies.

2.3 Relativistic jets

The twin jets are very highly collimated and as they propagate through the interstellar medium at relativistic speeds, they harbor a huge amount of kinetic energy.

There are two important observations which tell us that the jets could emanate from deep within the potential well of the accreting compact object and, therefore, are closely related to the accretion process itself. First, the speed of the jet is of the order of the escape velocity from the vicinity of the compact object. For example, the jets observed from the black hole candidate GRS 1915+105 move with a speed of $0.92c$ (Mirabel and Rodríguez 1994) which corresponds to the escape velocity at a distance of $2.4R_g$ from the compact object. Secondly, the jet ejection takes place during the state transition from the LH state to the HS state, and indicates a relationship between the jet and the accretion disk. This is often accompanied by the temporary disappearance of the hard X-ray emission which indicates the cessation of hard X-ray production in the corona.

Though it is clear that the black hole systems produce energetic and relativistic jets, they present a difficulty for the electromagnetic theory of jet production: black holes cannot support a magnetic field. The only way for supporting such a magnetic field is that the current generating the magnetic flux comes from an external supply of plasma, i.e. the accretion flow. On the other hand, accretion flows are believed to be weakly-magnetized plasmas in highly turbulent, rotating flows around the black hole (Balbus and Hawley 1998). Thus, managing a well-behaving, global and rotating magnetosphere with this turbulent accretion disk is a tricky problem. The leading model for producing this kind of phenomenon is called the magnetohydrodynamic (MHD) accelerator model which was originally proposed by Lovelace (1976) and Blandford (1976). Briefly, it uses energy from the differential rotation of the accretion disk coupled with a strong electromagnetic field to convert rotational kinetic energy into kinetic energy of a jet. A magnetic pressure gradient lifts the plasma out of the gravitational potential well and the pinch effect collimates the outflow into a jet. However, there are observational reasons for believing that the same source may produce jets of different speeds, either simultaneously or in different accretion states. Similarly, there are multiple theories for producing jet launching in the same black hole system. Two models that may be driving XRBs are known as the Blandford-Payne (Blandford and Payne 1982) and the Blandford-Znajek (Blandford and Znajek 1977) mechanisms. The former uses only Newtonian mechanics to drive axially-oriented outflows from the disk and the latter concerns the vicinity of the compact object and how in this region the magnetic field lines are forced, by the rotation of the disk, to spin. The spinning field lines will assume an outward spiraling shape and centrifugal forces will fling out the magnetically frozen plasma along the field lines to form two magnetized jets. The toroidal magnetic field will pinch the plasma towards the jet axis that provides self-collimation to the jets. It is also possible to extract energy from the spin of the black hole to drive the jet and achieve more energetic outflows (Punsly and Coroniti 1990). Supporting observations exists that show that the jet energies in the black hole systems are indeed ~ 30 times more strong than the jet energies in the neutron star systems with similar accretion rates (Migliari et al. 2003).

2.3.1 Jet ejection and major radio flares in Cygnus X-3

Unlike most other XRBs, Cygnus X-3 is relatively bright in the radio virtually all of the time and it undergoes giant radio outbursts with strong evidence of precessing jet-like structures (Fig. 2.8) moving away at relativistic speeds ($v \sim$ 0.6–0.8c) with an inclination of $\leq 14^{\circ}$ to the line-of-sight (Mioduszewski et al. 2001; Miller-Jones et al. 2004). Tudose et al. (2010) have shown that during the active states the radio emission from the jet dominates that from the core. Also, the radio emission does not show any orbital modulation therefore being consistent with the notion that the radio emission arises further out in the jet. Cygnus X-3 exhibits a power law of positive or negative slope in the radio, usually depicted as synchrotron radiation from the relativistic electrons in the jet. This synchrotron radiation may extend to infrared/optical wavelengths

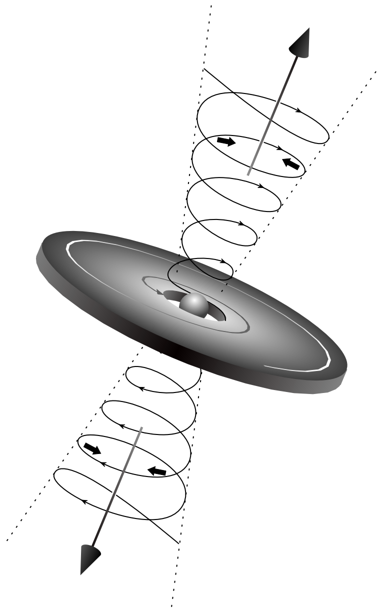

Figure 2.7. A schematic diagram depicting the MHD acceleration and collimation model. Magnetized and rotating inflow spiraling toward a compact object (white solid arrow) winds the magnetic field lines into a rotating helical coil. Magnetocentrifugal forces expel some of the material along the field lines and magnetic pressure and pinching forces (black short solid arrows) further lift and collimate it into a jet outflow (black long arrows).

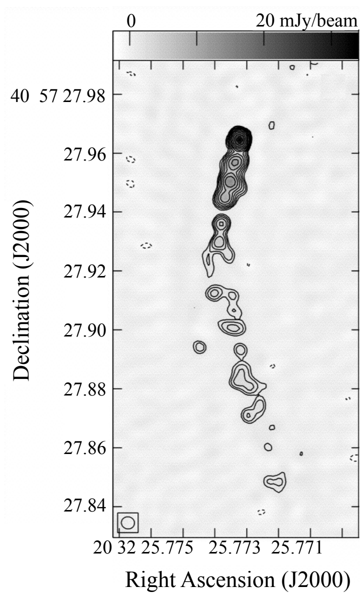

Figure 2.8. A Very Long Baseline Array images of Cygnus X-3, modified from Mioduszewski et al. (2001), showing a curved jet.

and even to X-rays and it could be optically thick or thin to synchrotron self-absorption.

The radio emission exhibits several correlations with the X-ray emission during a major flare episode. During times of moderate radio brightness ($\sim$ 100 mJy), and low variability in the radio and X-ray fluxes, the hard X-ray flux anti-correlates with the radio (McCollough et al. 1999). The major flaring episode begins when Cygnus X-3 descends into a radio/hard X-ray quenched state (denoted as the hypersoft state in Publication I), where the hard X-rays and radio switch from an anti-correlation to a correlation. This state will last from a couple of days up to a month. It is a rare state, comprising $\sim$ 2–3 % of the overall monitoring live time. Upon emerging from this state, Cygnus X-3 will always exhibit major radio flaring (Szostek et al. 2008) followed by flaring in the hard X-rays as well (McCollough et al. 1999). After the major flare decay Cygnus X-3 returns back to the LH state or it can loop again back to quenched state to produce another major flare.

2.3.2 γ-rays in Cygnus X-3

Cygnus X-3 has been detected by various space missions out to energies of $\sim$ 200–300 keV. Throughout the 1970s and 1980s there were reported detections of Cygnus X-3 in the MeV to PeV energy ranges (Vladimirsky et al. 1973; Danaher et al. 1981; Lamb et al. 1982; Samorski and Stamm 1983; Bhat et al. 1986), but none of these detections were confirmed or found to be reproducible (O'Flaherty et al. 1992; Hermsen et al. 1987; Mori et al. 1997; Aleksić et al. 2010). Recent observations by Astro-rivelatore Gamma a Immagini Leggero (*AGILE*) and *Fermi* have shown that the Cygnus region is a very complicated area at γ-ray energies. Cygnus X-3 has now been shown by both *AGILE* (Publication IV) and *Fermi* (Fermi LAT Collaboration et al. 2009) to be a γ-ray source ($>$ 100 MeV). Also, *Fermi* observations show that the γ-ray emission exhibits the same 4.8 hour modulation as in X-rays and infrared attributed to orbital modulation, thus resulting in the firm association of γ-rays with Cygnus X-3. Interestingly, the peak of the γ-ray emission occurs near phase 0.0 at the far side of the WR star. The peak isotropic luminosity above 100 MeV is $L_\gamma \sim 10^{36}$ erg/s.

γ-rays have also been detected outside of major radio flare episodes and have been associated with very brief periods of hard X-ray quenching and minor radio flaring (Corbel et al. 2012). In one case the hard X-ray quenching lasted only $\sim$ 0.5 day and in the other for a day. In the last period of activity a 1 Jy radio flare (at 15 GHz) was observed during the period of γ-ray emission (Bulgarelli et al. 2012). γ-rays are reported to occur also without associated radio emission Williams et al. (2011).

It is still under debate whether the γ-rays arise from leptonic (Dubus et al. 2010; Zdziarski et al. 2012b; Piano et al. 2012) or hadronic processes (e.g. Romero et al. 2003; Piano et al. 2012). The leptonic scenario is based on the inverse-Compton scattering of soft stellar photons by the relativistic electrons in the jet that are streaming towards us close to the line-of-sight. The interaction of the jet with the stellar photon field close to the compact object (within ten orbital separations) scatters the photons up to MeV energies. The hadronic scenario, where the jet is populated with protons, is based on the proton-proton collisions that occur between the protons in the hadronic jet and the protons in the stellar wind. The collisions produce pions and γ-rays via the decay of neutral pions. In addition, the jet origin of the γ-rays is still debatable as Williams et al. (2011) present some evidence against the model of inverse-Compton scattering of soft stellar photons by the jet.

In this chapter the mechanisms responsible for producing the emission from Cygnus X-3 throughout the electromagnetic spectrum have been briefly introduced and how they connect to previous observations. In the next chapter the observatories used to obtain the data analyzed in this thesis are introduced, as well as the analysis methods used to extract information from the data.

3. Materials and methods

3.1 Observations

A large set of multiwavelength observations of Cygnus X-3 from ground- and space-based observatories is used in this thesis. The main focus lies in the analysis of the radio and X-ray data, but supporting observations from ultraviolet/optical, infrared and γ-ray data are taken into an account. In the following, the main instruments involved are introduced.

3.1.1 Radio observatories

Before its decommissioning in 2000, the **Green Bank Interferometer (GBI)** included three 26-meter-diameter radio telescopes operated by the National Radio Astronomy Observatory with support from the National Aeronautics and Space Administration (NASA) High Energy Astrophysics program at its Green Bank site in West Virginia, United States. The telescope had an angular resolution of about 3 arcseconds and 11 arcseconds in its two operating frequency bands, 8.3 GHz and 2.25 GHz, respectively. The root-mean-square noise in a 5-minute scan is about 6 mJy at 8.3 GHz and 10 mJy at 2.25 GHz. The data used in this thesis were obtained via ftp://ftp.gb.nrao.edu/pub/fghigo/gbidata/gdata/2030+407.

The **Arcminute Microkelvin Imager Large Array (AMILA)**, operated by the Cavendish Astrophysics Group, is composed of eight 12.8-meter-diameter, equatorially mounted Cassegrain antennas, which were previously part of the Ryle Telescope (decommissioned in 2006) located at the Mullard Radio Astronomy Observatory in Lord's Bridge near Cambridge, England. The antennas are separated by distances ranging between 18 and 110 m. The telescope has an angular resolution of approximately 30 arcseconds with a flux sensitivity 3 mJy $s^{-1/2}$ and it operates at six frequencies between 13.9–18.2 GHz (AMI Consortium: Zwart et al. 2008). 15 GHz monitoring data of Cygnus X-3 is used in this thesis (Publication I; Publication IV).

The **RATAN-600** (or the Academy of Science Radio Telescope) is a reflector-type radio telescope operated by the Special Astrophysical Observatory of the Russian Academy of Science located near the village of Nizhny Arkhyz, Russia. The main mirror of the telescope was built in the shape of a ring with a diameter of 577 meters, containing 895 individual elements with dimensions of 2 meters times 11.4 meters. The individual elements reflect the radiation either toward a central conical receiver or to one of five cylindric reflectors, that in turn direct the converging beam to the secondary mirror, which collects the radiation at the focus where the primary receiver feeds are located. The RATAN-600 has a maximum angular resolution of 2 arcseconds with a flux density limit of 0.5 mJy. It operates in the frequency range 0.61–30 GHz. Monitoring data from Cygnus X-3 in seven frequency bands (1.0, 2.3, 4.8, 7.7, 11.2, 21.7 and 30 GHz) is used in this thesis (Trushkin et al. 2008, Publication I).

3.1.2 X-ray observatories

The **Rossi X-ray Timing Explorer (*RXTE*)** was an X-ray satellite operated by NASA/Goddard Space Flight Center, decommissioned in 2012, consisting of three X-ray instruments: the All-Sky Monitor (ASM, Levine et al. 1996), the Proportional Counter Array (*RXTE*/PCA, Jahoda et al. 1996) and the High Energy X-ray Timing Experiment (HEXTE, Rothschild et al. 1998). The ASM scanned about 80% of the sky every orbit at a spectral range 2–10 keV down to a sensitivity of about 10 mCrab. The *RXTE*/PCA and HEXTE were pointing instruments which cover spectral ranges 2–60 keV and 15–250 keV with an energy resolution below 18% at 6 keV and 15% at 60 keV respectively. The *RXTE*/PCA consisted of five xenon gas proportional counter units (PCU) with a throughput of $\sim$ 2500 counts/s/PCU when observing the Crab Nebula, background of 90 mCrab and time resolution 1 μs. The HEXTE consisted of two clusters of scintillation detectors with a sensitivity of $\sim$1 mCrab for 100 ks observation, background 50 counts/s/cluster and time sampling rate 8 μs. The *RXTE* data used in this thesis were obtained from the High Energy Astrophysics Science Archive Research Center (HEASARC).

Swift (Gehrels et al. 2004) is a space-based multiwavelength observatory operated by NASA/Goddard Space Flight Center that includes three instruments onboard: the Burst Alert Telescope (BAT) operating in the 15–150 keV hard X-ray band, the X-ray Telescope (XRT) operating in the 0.3–10 keV soft X-ray band, and the UV/Optical Telescope (UVOT) operating in the wavelength range 170–650 nm. The BAT is a coded aperture mask instrument that has a large field-of-view of 1.4 steradians. It is used to monitor the hard X-ray sky with a sensitivity of $\sim$ 2 mCrab in 16 hours exposure time and with a spectral resolution of $\sim$7 keV. The XRT is a focusing X-ray telescope with 110 cm^2 effective area, 23.6 $\times$ 23.6 arcminutes field-of-view and 18 arcsecond resolution. The spectral resolution at launch was $\sim$ 140 eV at 6 keV. The UVOT is a diffraction-limited 30 cm Ritchey-Chrétien reflector, sensitive to magnitude 22.3 in a 17 minute exposure in B filter. The *Swift* data used in this thesis were obtained from the HEASARC.

The **International Gamma-Ray Astrophysics Laboratory (*INTEGRAL*)** is an international space-based multiwavelength observatory in a highly eccentric orbit designed to observe the sky in the optical, X-ray and γ-ray wavelengths. It is operated by the European Space Agency in cooperation with the Russian Space Agency and NASA. *INTEGRAL* hosts four instruments onboard: the Imager on-Board the *INTEGRAL* Satellite (IBIS, Ubertini et al. 2003) that observes from 15 keV to 10 MeV, the Spectrometer on *INTEGRAL* (SPI, Vedrenne et al. 2003) that observes from 20 keV to 8 MeV, the Joint European X-ray Monitor (JEM-X, Lund et al. 2003) that observes from 3 keV to 35 keV, and the Optical Monitoring Camera (Mas-Hesse et al. 2003) sensitive to radiation in the wavelength range 500 to 580 nm. IBIS is a coded-mask instrument featuring two detector layers: the hard X-ray detecting layer *INTEGRAL* Soft Gamma-Ray Imager (ISGRI, Lebrun et al. 2003) and the γ-ray detecting layer Pixellated Imaging Caesium Iodide Telescope (PICsIT, Di Cocco et al. 2003). IBIS has 12 arcminutes angular resolution with 8.3 $\times$ 8.0 degree fully coded field of view, time sampling rate of 61 μs and a spectral resolution of 8% at 100 keV (ISGRI) and 10% at 1 MeV (PICsIT). SPI is a coded-mask instrument with 2.5 degree angular resolution, 16 degree fully coded field of view and energy resolution of 2.2 keV at 1.33 MeV. Like IBIS and SPI, JEM-X is also a coded-mask instrument. It has

4.8 degree fully coded field of view, 3 arcminute angular resolution, 1 ms time sampling rate and a spectral resolution of 1.3 keV at 10 keV.

3.1.3 γ-ray observatories

Astro-rivelatore Gamma a Immagini Leggero (*AGILE*) is a multiwavelength observatory operated by the Italian Space Agency that includes two instruments: the Gamma-Ray Imaging Detector (GRID, Barbiellini et al. 2002; Prest et al. 2003) sensitive to photons with energies 30 MeV – 30 GeV with the optimal range from 0.1–1 GeV, and the Super-AGILE detector (Feroci et al. 2007) sensitive to photons with energies 18–60 keV. The GRID allows γ-ray source positioning with error box radius near 5–20 arcminutes and it is designed to achieve a nominal spectral resolution of $\delta E/E \sim 1$ at 200 MeV. *AGILE* operates in a fixed-pointing mode, implying that it can accumulate data on a source within its large field of view (2.5 steradians for the GRID) fourteen times a day, taking into account Earth occultations during each spacecraft orbit. *AGILE* monitoring observations of Cygnus X-3 are used in this thesis in Publication IV.

3.2 Analysis methods

3.2.1 The hardness-intensity diagram with simultaneous radio flux density measurements as a probe to study the disk-jet connection

The "disk-jet connection" concept consists of studying the relation between the accretion disk (emitting mostly in the X-rays) and the jet (emitting mostly in the radio). In general, many bright XRBs are accompanied during an X-ray outburst by a radio outburst (Fender et al. 2009). Thus, is is apparent that rapid changes in the disk configuration and mass accretion rate that cause X-ray state changes are also coupled with the jet production. In the case of persistent XRBs, like Cyg X-1, the X-ray and radio are correlated during the LH state (e.g. Zdziarski et al. 2011). But when the system transitions from the LH to the HS state, the radio emission quenches abruptly. However, there is evidence that an unresolved compact jet is present in the HS state at least for Cyg X-1 (Rushton et al. 2012). Again, the state transition is linked to the major changes in the accretion geometry which prevents the jet production (e.g. Tigelaar et al.

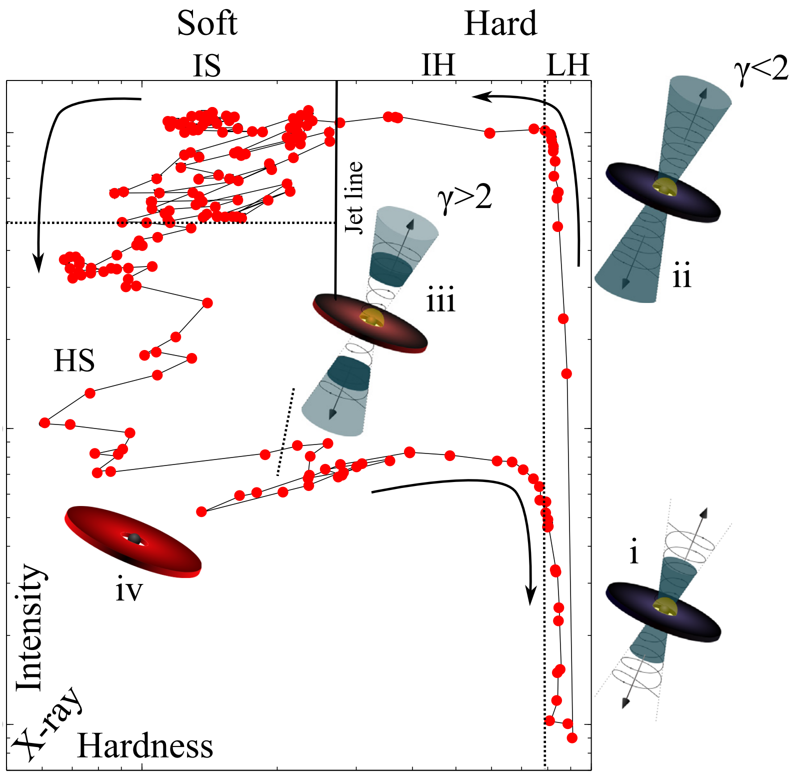

Figure 3.1. A simplified model for the disk-jet connection in XRBs showing an X-ray HID of GX 339−4 (Belloni et al. 2005) together with sketches of the accretion states (marked with roman numerals) depicting the components of the system: the jet, the accretion disk and the corona. In the HID the logarithm of X-ray hardness ratio is plotted against the logarithm of X-ray bolometric intensity (3–200 keV). The spectral evolution of GX 339-4 (other XRBs show very similar behavior) is shown to progress from the LH state (right), through the intermediate states (IH/IS) to the HS state (left) and descending back to the LH state. In the LH and IH states the jet is steady with an almost constant bulk Lorentz factor typically of $\gamma < 2$, progressing from the accretion state **i** to state **ii** as the intensity increases. During these states the disk is cold and the coronal emission is dominating the X-ray spectrum. When the system crosses the so called "jet line", Lorentz factor of the jet rapidly increases producing an internal shock in the outflow (**iii**) followed in general by cessation of jet production (albeit some fading optically thin radio emission can be detected from the jet/shock, which is now physically decoupled from the central engine). It it possible for XRB to loop around the jet line multiple times producing further optically thin radio outburst but only when crossing the line from right to left. At the same time the source spectrum starts to be dominated by the disk emission and eventually it moves to the HS state with hot disk, no jet and very little, if any, coronal emission (**iv**).

2004). Thus, it is the "intermediate state", often subdivided into multiple (sub-)states, that conveys important information regarding the disk-jet connection, since it lies between the two extreme states. Typically, XRBs follow a similar evolution through the different X-ray spectral states and trace similar tracks in the HID (Fig. 3.1). A typical black hole HID representing the transient outbursting cycle has a Q-type shape that can be divided into four main areas or states: quiescent, low/hard, intermediate and high/soft. These areas/states are briefly reviewed in the following:

Quiescent state (lower right in the diagram): The source flux is very low in both the X-ray and radio with the spectrum described by a hard power law;

Low/hard (LH, right side): The source can be bright in the X-rays and its spectrum is described by a power law with exponential cut-off at ~ 100 keV. The radio emission has a flat spectrum and appears as a compact jet;

Intermediate (top): As the source moves from the LH state to the intermediate state the radio emission stays steady almost until the point of major ejection in the intermediate/soft (IS) state. However, the radio emission starts to become more variable exhibiting a peaked or optically thin spectrum shortly before the radio flare, which occurs during the state change from the intermediate/hard (IH) state to the IS state. Also, when the source moves in the opposite direction, from the IS to the IH, this often corresponds to optically thin radio outbursts (Fender et al. 2004). Jets during the intermediate states are associated with highly relativistic motion, unlike the steady jets in the LH state which are usually mildly relativistic. This implies that the geometrical change in the disk could cause a more energetic jet than it would otherwise. One scenario to explain this behavior invokes internal shocks. The increase of the X-ray luminosity of the accretion source could result in the increase of the velocity of the outflow. Thus, the more energetic jet (with greater velocity) catches up with ejecta in the jet that were emitted in the LH/IH state and forms shocks. During this state there is a prominent thermal disk component and a steep power law without a cut-off;

High/soft (HS, left side): This state is thermally dominated and typically there is no power law component, or if present, it is very weak. There is also a line that demarcates the intermediate state region from the HS region that is referred to as the *jet line*. When the source crosses this line going from right to left there is a sudden cut-off of radio emission. It is during this transition that strong radio flares occur.

The overall picture emerging from the disk-jet connection and theoretical studies of jet launching (see Section 2.3) is that in the LH state (phase **i** in Fig. 3.1) the jet is powered by the Blandford-Payne mechanism, i.e. the accretion disk powered jet, resulting in a steady but rather weak jet. On the other hand, as the system transits to intermediate X-ray states the accretion disk propagates inward and the plasma starts to "feel" the compact object and the jet gains more energy via the Blandford-Znajek mechanism. When the disk approaches the ISCO, the Lorentz factor of the jet increases rapidly (see Fig. 3.1) before the jet is suppressed in the HS state. This may occur due to the suppression of the jet launching mechanism or due to a suppression of the radio emission. An example of the former could be a shift in the accretion geometry from a thick disk to a thin disk, which would strongly affect the magnetic field strength driving the jet. An example of the latter could be the interaction of the non-thermal, synchrotron-emitting particles with the strong radiation field of the disk slowing down the relativistic particles and producing thermal jets. Thus, major radio flaring periods are of prime importance for studying the relationship between the accretion disk and the radio jets, using simultaneous radio and X-ray observations.

3.2.2 Simulating power law noise and deriving a reliable QPO signal with Monte-Carlo techniques

X-ray QPOs are one of the prime observation tools for probing the strong gravitational field near the compact object in XRBs. They range from a low frequency regime of mHz variations to a high frequency regime of kHz variations bounded by the light crossing time of the emission region. The rapid variations in the X-ray lightcurve are essentially stochastic processes and can be described best with statistical tools. This variability is usually in the form of a power law in the Fourier transformed frequency space spanning a large continuous set of frequencies $P_\nu(\nu) \propto \nu^{-\alpha}$, where P_ν is the power density associated with a frequency ν. Often this broad structure is referred to as the "noise" component. In addition to the noise, the PDS can contain a peak around a specific frequency ν_0 that can be modeled with a Lorenzian profile $P_\nu \propto \mathrm{FWHM}/[(\nu - \nu_0^2) + (\mathrm{FWHM}/2)^2]$, where FWHM is the full width at half maximum of the peak. The Lorentzian in the power density spectrum corresponds to an exponentially damped sinusoid in the lightcurve (although the underlying signal may be something different as well), thus being a quasi-periodic oscillation with the usual convention that the quality factor $Q \equiv \nu_0/\mathrm{FWHM}$ which measures the coherence of the peak is larger than two (van der Klis 2006).

A noise component with $P_\nu(\nu) \propto \nu^{-2}$ power spectrum is often referred to as *red noise*. Red noise is known to produce low-frequency peaks in the PDS and thus any low-frequency QPO candidate found in the red noise dominated PDS has to be considered carefully and should be compared to properties of randomly generated lightcurves (Benlloch et al. 2001).

One good method is to produce randomly generated lightcurves with similar characteristics as the original lightcurve, i.e. the same length and mean counts of the lightcurve, and power law index of the PDS derived from the lightcurve. On the basis of a large number of simulated lightcurves, confidence limits can be placed for each frequency corresponding to how many times the simulated lightcurves reached a given power density in a given frequency. This method is by definition a Monte-Carlo calculation. Typically, any peak below a confidence level of 99% or, preferably, 99.9% is considered as being part of the noise (Bevington and Robinson 1992).

One algorithm for generating simulated power law noise lightcurves is depicted in Timmer and Koenig (1995). It is based on a linear theory of stochastic processes, where the Fourier transform $f(\nu)$ is a complex gaussian random variable determined by the spectral density distribution:

$$f(\nu) = \mathcal{N}[0, \frac{1}{2}P(\nu)] + i\mathcal{N}[0, \frac{1}{2}P(\nu)], \tag{3.1}$$

with a variance that does not depend on the number of data points. The individual steps for the algorithm goes as follows:

- Choose a spectrum and take the square root of $\sqrt{P(\nu)}$

- Draw two Gaussian-distributed random number sets with length equal to the number of frequencies in the spectrum, zero mean and standard deviation equal to one and multiply them with $\sqrt{P(\nu)}$

- Allocate the Fourier transform $f(\nu)$ with positive and negative frequencies equal to the number of frequencies in the spectrum

- Populate the Fourier transform $f(\nu)$ real and imaginary part for positive frequencies with the random number sets drawn above

- Make sure that the Fourier transform is real at the Nyquist frequency $f(\nu_{Nyquist}) = 0.0$

- Populate the Fourier transform real and imaginary part for negative frequencies using $f(-\nu) = f^*(\nu)$, where the asterisk denotes complex conjugation

- Collect all parts (real and imaginary) to form the Fourier transform $f(\nu)$

- Make transform into time domain using fast Fourier techniques and drop the imaginary part

- Normalize lightcurve to match the original one

3.2.3 Principal component analysis as a tool to unite timing and spectral information

The main use of principal component analysis (PCA) is to find the smallest number of components that suffice to explain the data losing the least amount of information in the process. Basically, PCA finds patterns in the data in a way that highlights the differences and similarities in the data set. In many-dimensional cases, when graphical representation is not convenient, it is a particularly powerful analysis tool. By finding the "new coordinates" of the data set (i.e. the principal components) where the data points mainly cluster and ignoring the small scatter that the data points have around these coordinates the dimensionality of the data set is reduced greatly, defined only by these new coordinates.

Here, we briefly summarize the main points of the analysis using X-ray spectra as input and relating that to a simplified example depicted in Fig. 3.2:

- Start with a number of spectra p measured at times t_1, t_2, $\ldots t_p$ binned into n bins corresponding to energies E_1, E_2, $\ldots E_n$. In Fig. 3.2 one data point would correspond to one energy spectrum. However, in this case the data points have just two energy bands (x and y), while usually the spectra would include at least ten different bands to get a feeling of the shape of the spectrum. The number of data points in the example would

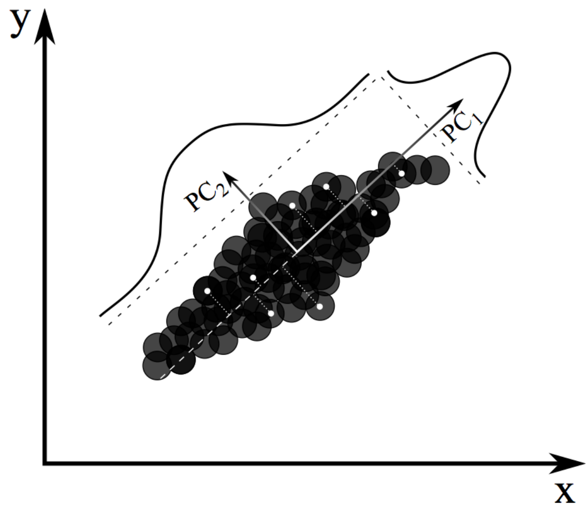

Figure 3.2. A simplified, graphical example of how the PCA works. The principal components can be though of as a new coordinate system with the origin at the mean data value and the axes rotated so that the first principal component points to a direction where most of the data are oriented. By definition the principal components are orthogonal to each other. In order to reduce the degrees of freedom (i.e. noise) from the data, the data points can be projected on to a smaller set of principal components. E.g. in the figure the data points are projected to the line defined by the first principal component.

correspond to the number of spectra p.

- Form a $p \times n$ matrix with coefficients $F(t_p, E_n)$, i.e. the fluxes in each energy band at times p. In the example this would be a matrix with two columns for the values x and y and the number of rows equal to the number of data points.

- Subtract a mean flux $\bar{F}(E_n)$ from the coefficients for each energy channel.

- Compute the $n \times n$ covariance matrix out of the data matrix, which states the variances (in the diagonal) and covariances (elsewhere) between each energy bands.

- Calculate the eigenvectors, s_n, and eigenvalues of the covariance matrix. These eigenvectors form the new coordinates of the data and the accompanying eigenvalue states the proportion of variance of a particular eigenvector, i.e. the highest eigenvalue and accompanying eigenvector is the first principal component of the data set etc. In the example these would refer to the new coordinates PC_1 and PC_2.

- Form a linear decomposition $S_{nk} = (s_{n1}s_{n2}\dots s_{nk})$ of the data set using the above eigenvectors, ordered by the proportion of variance. The components producing only a small fraction of the overall variance can be then dropped off, reducing the dimensionality, i.e. choosing a small number of eigenvectors for the linear composition. In the example the data shows biggest variance in the direction of PC1.

- The data set defined by the new coordinates can be obtained by

$$F_{kp} = S_{kn} \times \bar{F}_{np} = \sum_{i=1}^{n} S_{ki}\bar{F}_{ip} \qquad (3.2)$$

  Where the chosen k coordinates lie in direction of the calculated eigenvectors s_k. In the example this can be visualized by rotating the original coordinates and transferring the origin to the mean of x and y so that they correspond to the coordinates of PC1 and PC2.

- The original data set without the less significant components, which most likely are just systematic errors and noise, can be obtained via

$$F_{np}^{PCA} = (S_{nk} \times F_{kp}) + \bar{F}(E_n) = \bar{F}(E_n) + \sum_{i=1}^{k} S_{ni}F_{ip} \qquad (3.3)$$

  leaving only the intrinsic variability in the data set. In the example this refers to projecting the data points onto the PC1 axis.

One of the most interesting avenues to follow in the subsequent analysis of the principal components is to track the evolution of F_{kp} for each k (that produces most of the overall variance) with time t_p. Identifying this evolution with the change of spectral fit parameters performed on the original energy spectra can give us clues as to which spectral component or a parameter of that component could be the source of the variability attributed to the principal component s_{nk} for chosen k:s.

In this chapter the observatories used to obtain the data in this thesis were introduced together with the three most important methods to analyze this data. The results of these analyses are presented in the following chapter.

4. Results

4.1 The disk-jet connection and spectral states

In Publication I, a more complete HID is constructed with the help of an extensive data set from *RXTE*. In addition, during most of the *RXTE* observations there are (near-)simultaneous radio observations from the GBI, AMILA and RATAN-600 radio telescopes. In the spirit of the original HID design where the jet emission phases are depicted (connected to radio emission via synchrotron radiation), Publication I presents the HID of Cygnus X-3 with the simultaneous radio flux densities plotted on top of the X-ray hardness-intensity plot (Fig. 4.1). In this way the connection between the X-ray emission, both soft (from the accretion disk or from some other thermal emission process) and hard X-rays (from inverse-Compton scattering), and radio emission from the synchrotron process in the jet become clearer. The radio emission demarcates the HID into three separate regions: LH X-ray state with quiescent radio emission levels ($\sim$ 100 mJy), intermediate X-ray state with radio flaring (0.3–20 Jy), and HS X-ray state with quenched radio emission. Due to the complexity of Cygnus X-3's X-ray spectra, they have been classified into many different substates in previous studies (Szostek et al. 2004; Szostek and Zdziarski 2008; Hjalmarsdotter et al. 2009). However, the region in the HID that encompasses the HS X-ray state with the quenched radio emission does not correspond well to any of the previously determined states as it exhibits even softer X-ray spectra than the softest state in Szostek et al. (2004); Szostek and Zdziarski (2008) called this the ultrasoft state. In addition, the behavior of Cygnus X-3 between the softest state, dubbed the "hypersoft" state in Publication I, and the intermediate/flaring state exhibits very interesting phenomena. This region corresponds to the jet

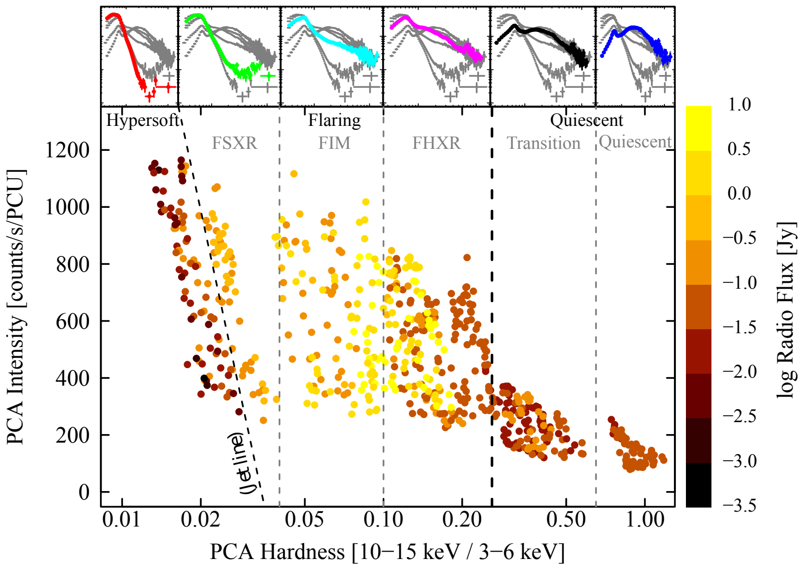

Figure 4.1. Cygnus X-3 hardness-intensity diagram with the simultaneous radio flux densities (the darker color referring to lower flux) plotted on top of the X-ray data points. The plot is divided into six different areas which correspond to six different X-ray states of Cygnus X-3 (see Fig. 2.6, same coloring scheme used). The corresponding X-ray state spectra are plotted in the upper part of the figure, each above its own area. The division between the hypersoft state and the FSXR state is labeled the jet line. When Cygnus X-3 crosses this line *from* the hypersoft state, it produces a major flare. However, no flares have been observed when the system crosses the line in the other direction.

line in the original HID, but the behavior of Cygnus X-3 across this line is observed to be the opposite compared to other XRBs/microquasars: when Cygnus X-3 crosses the jet line from right to left, radio jet ejections are *not* observed and the source just quenches into the hypersoft state. However, when the source exits the hypersoft state a major radio flare is *always* observed. In addition, when Cygnus X-3 crosses the jet line, i.e. moving into or out of the hypersoft state, a burst of γ-ray emission is detected (see Section 2.3.2).

However, major flares differ depending on how strong the accompanying hard X-ray flare is (Publication I). Variations can also occur within the same flaring episode. After reaching the peak radio flux density of the major flare, the X-ray spectra evolve from soft to hard (Szostek and Zdziarski 2008, Publication I) with a rising non-thermal tail in the X-ray spectra (i.e. FSXR–FIM states) until the tail exhibits a cutoff (FHXR state). However, the FHXR and FIM states can occur in the opposite order after the peak of the major flare.

4.2 Low-frequency QPOs and the jet

In Publication II, the search method for QPOs described in Section 3.2.2 was used to analyze the whole *RXTE* archive (at the time of publication) including all X-ray spectral states to search for low-frequency QPOs (< 0.1 Hz). This extensive search resulted in *two* detections above the 99.9% confidence level, further reinforcing the short-lived and sporadic nature of these events. In addition, both of these detections as well as the previous ones in van der Klis and Jansen (1985) and Rao et al. (1991) are associated to a certain extent with major radio flaring events (Publication II;Publication VI). This result brings forth scenarios where the jet or some structure in the jet is responsible for modulating the underlying emission or causing the QPOs itself and thus broadening our notion of where the QPOs originate.

4.3 Spectral components during an outburst

In Publication III PCA was performed on the X-ray spectra from *RXTE*, *INTEGRAL* and *Swift* during a major flare ejection event in May–July 2006. The analysis showed that there are two main variability compo-

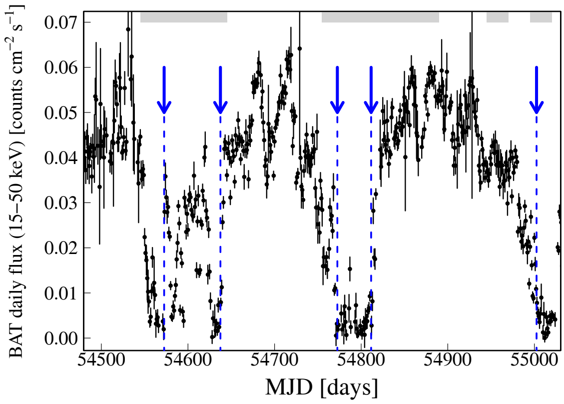

Figure 4.2. The *Swift*/BAT ligthcurve with *AGILE* coverage (shaded grey bars) with the GeV detections (blue arrows). Note the occurrence of γ-ray detections in every local minimum of the hard X-ray lightcurve.

nents in play, i.e. two principal components accounted for almost all the variability in the X-ray lightcurves. According to the spectral shape of these components and spectral fits to the original data, the most probable emission components corresponding to the principal components are inverse-Compton scattering and bremsstrahlung. In addition, during the major flare ejection a plausible scenario of bremsstrahlung photons inverse-Compton scattering off of relativistic electrons in the jet is supported by the analysis.

4.4 The link between γ-ray emission and spectral states

The γ-ray emission is associated with specific times characterized by low hard X-ray flux, low radio flux and high soft X-ray flux. A strong anti-correlation exists between the γ-ray emission and the hard X-ray emission, and it appears that every local minimum in the hard X-ray lightcurve (*Swift*/BAT count rate <0.02 counts cm^{-2} s^{-1}) corresponds to a time when γ-ray emission is detected from the system (Fig. 4.2). Likewise, during the periods of γ-ray emission the *RXTE*/ASM count rate exceeds the transitional value of 3 counts/s (Szostek and Zdziarski 2008). Thus, the X-ray/radio state that corresponds to the above correlations is the hypersoft state. The γ-ray flares are observed during the declining phase as well as the rising phase to/from the hypersoft state (Publication IV). The hypersoft state is almost always associated with a major radio flare and therefore a jet ejection event. When the source leaves the hypersoft state a major radio flare with a radio flux density of several Janskys is detected. This ties in the γ-ray emission with the jet and it is very plausible that the source of the γ-rays *is* the jet, as no other component in microquasars is known to be responsible for generating copious numbers of relativistic particles. Thus, the following sequence of events always takes place during a major radio flare event: the source transits into the hypersoft state producing γ-rays, and then remains in the hypersoft state with little or no radio nor hard X-ray emission for approximately ten days up to one month until it again flares in γ-rays; a few days after the appearance of the γ-ray emission, the source abruptly brightens in the radio by several orders of magnitude, signaling a jet ejection event, in conjunction with the recovery of the hard X-ray emission. Studying this unique sequence of events opens up a new avenue to exploring how the accretion disk, the corona, and the jet are inter-connected.

5. Discussion

Despite having been studied for 46 years at all wavelengths throughout the electromagnetic spectrum, Cygnus X-3 still has a few surprises up its sleeves as this thesis shows. With the advent of high-precision space-based γ-ray observations we have seen that microquasars do indeed live up to their multiwavelength nature as most recently manifested by the detection of γ-ray emission from Cygnus X-3, but it could be that to truly fulfill this criterion special conditions need to be met in order to extend up to the GeV level. In addition, despite the heavy damping of the X-ray timing signals a few low-frequency QPOs are detected which are interestingly coincident with the major flaring episodes. The soft X-ray emission from Cygnus X-3 could represent the characteristics of bremsstrahlung emission, which is a relatively rare emission process in the microquasar scenario. But do these findings present a more unified picture of Cygnus X-3 or do they merely offer more mysteries to be solved by further research? As necessary when regarding the essence of science, it is a bit of both.

5.1 Implications

A key element in the observations of all the above-mentioned "surprises" is to look at Cygnus X-3 at the right time – the "right" time being restricted to a major radio flare, the messenger of a jet ejection event. Thus, it appears that the jet is the culprit, or at least partly responsible for the unique properties of Cygnus X-3. The order of the events during a major flaring episode is as follows (Fig. 5.1):

I: Decline to radio quenched i.e. hypersoft state with γ-ray flares (though the latter are not always present).

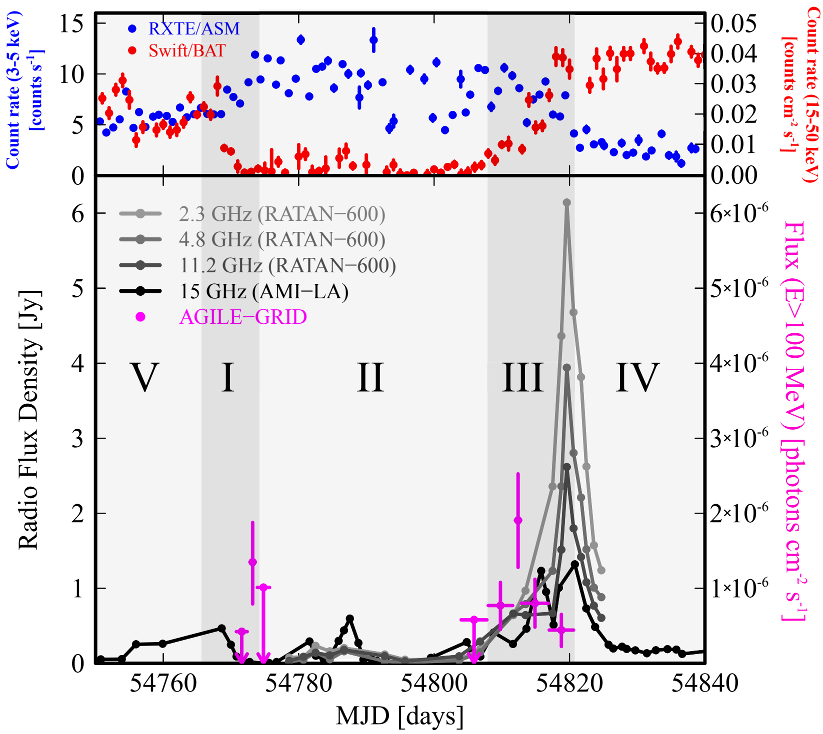

Figure 5.1. Multiwavelength campaign from Piano et al. (2012) including X-ray monitoring from *RXTE*/ASM and *Swift*/BAT in the upper panel, and radio monitoring from AMI-LA and RATAN-600 and γ-ray monitoring from AGILE-GRID in the lower panel. Roman numerals mark the sequence of events described in the text.

II: Hypersoft state characterized by low/non-existent levels of radio/hard X-ray emission. This stage lasts from about ten days up to a month.

III: Rapid rise of radio emission with γ-ray flares accompanied with the return of hard X-ray emission. Jet appears in the radio imaging.

IV: After the radio peak the X-ray spectrum hardens and the radio declines or continues to produce more flares. QPOs are detected in a few major flaring episodes at this stage.

V: Eventually the flaring episode powers down to a quiescent state where Cygnus X-3 can remain for years until the next outburst.

What is remarkable about Cygnus X-3 is that the sequence of events described above appears to operate backwards when compared to other XRBs/microquasars. No major radio flares have been observed when Cygnus X-3 transitions to its softest state which is normally the case for other XRBs/microquasars. However, γ-ray flares are observed during this time and thus they might convey information on the birth of the jet. What remains to be solved in this scenario is why the radio emission lags the γ-ray emission by 10–30 days.

The correlation between the radio and hard X-ray emission has been established in McCollough et al. (1999), where positive correlation was found during radio flaring (including the radio quenched/hypersoft state) and negative correlation during the quiescent state. Publication I showed that the X-ray intensity increases by a factor of 2–3 when the source transits to flaring states. The dominant emission process in the hard X-rays is Comptonization as demonstrated in Publication I and Publication III, and thus it seems plausible to assume that the jet is producing the hot population of electrons required for Comptonizing the seed photons.

As all the jet launching mechanisms are dependent upon the existence of an accretion disk, one of the most natural places for the soft seed photon population is from the accretion disk. However, multiple soft seed population are possible and are hinted at in Publication III, where a bremsstrahlung component produced the best match for producing part of the soft X-ray emission (together with Comptonization). In any case a hot, thermal component was needed to fit the spectra and produce the spectral evolution of the principal components. Similarly, hot thermal components have been found to be necessary in order to fit well the intermediate X-ray spectra of microquasars GRS 1915+105 (Titarchuk and Seifina 2009; Mineo et al. 2012) and SS 433 (Seifina and Titarchuk 2010), and LMXRBs GS 2000+25, GS 1124−68 and XTE J1550−564 (Życki et al. 2001). This implies that perhaps multiple soft photon populations are needed to fit the spectra of other microquasars/XRBs as well. On the other hand, these systems do not contain a massive stellar wind emanating from the companion star as in the case of Cygnus X-3. One option could be that an accretion disk wind in these other systems could mimic the effect of a stellar wind. Likewise, it would be possible that a massive disk wind is mimicking the WR-phenomena for Cygnus X-3, but so far no such model exists.

Still another characteristic unique to Cygnus X-3 is that the jet axis appear to be aligned or close to the line-of-sight. Mioduszewski et al. (2001) found that the jets are inclined 14 degrees to the line of sight and precessing. Reinterpreting the archival Very Long Baseline Interferometry images, Miller-Jones et al. (2009) showed that the jets can change their position angle by 180 degrees with time which is in support of the precession and the jet axis lying close to the line-of-sight. Based on modeling the γ-ray emission and its orbital modulation Dubus et al. (2010) arrived at jet parameters that lie close to the line-of-sight. These studies show that Cygnus X-3 is more likely a "microblazar" than a microquasar. This notion could help in understanding the brightness in the radio during major radio flares as moderate beaming likely takes place (Miller-Jones et al. 2004; Lindfors et al. 2007). The "blazarness" of Cygnus X-3 might also explain the origin of the low-frequency QPOs during major flaring episodes. The QPOs could be caused by some structure in the jet emitting X-rays, e.g. a shock. Rani et al. (2010) have shown that low-frequency QPOs could occur in blazars in a turbulent region behind a shock where dominant eddies with turnover times corresponding to the QPO periods could explain the short-lived, quasi-periodic fluctuation. On the other hand, Vilhu and Hannikainen (2013) discussed a scenario where the jet forms clumps which end up trailing the jet and are advected together with the stellar wind to larger distances. This trail of clumps could cause flickering of the underlaying X-ray emission and thus cause quasi-periodic fluctuation. An interesting aspect of this model is that the projection of this clumpy trail onto the orbital plane places it in the phase interval 0.3–0.4, exactly the same phase interval where the low-frequency QPOs were observed in Publication II. This interval also exhibits an increase in the overall X-ray variability predominantly in the harder X-ray states (FIM/FHXR) observed during radio flaring. These states can be attributed to times when jet ejection is observed while a softer X-ray state (FSXR) might indicate a failed jet (Publication I). Whether or not the clumpy trail turns out to be a plausible model, it nevertheless gives more credit to the jet origin of the low-frequency QPOs.

The nature of the compact object in Cygnus X-3 has been debated ever since its discovery with proponents in favor of a neutron star or a black hole as the compact object. The galactic matter along the line-of-sight absorbs optical wavelengths and thus little is known about the inclination and the mass function of Cygnus X-3. With the help of radial velocity measurements of X-ray emission lines a separate case can be drawn for neutron star or black hole alternatives (Publication V) with high inclination ($\sim$60 degrees) for the neutron star case and low inclination ($\sim$30 degrees) for the black hole case. Low inclination is supported by studying the orbital modulation with infrared (Publication V) and X-ray data (Zdziarski et al. 2012a). Low inclination also fits well with the low inclination of the jet assuming that the accretion disk is mostly aligned with the orbital plane and the jet axis is mostly perpendicular to that. The mass estimates for the black hole range between 2.8–8.0 $M_\odot$ (Publication V) and 1.3–4.5 $M_\odot$ (Zdziarski et al. 2013). While the low end of these ranges overlap the allowed neutron star masses the black hole case is further strengthened with the similarity of the X-ray spectral states of Cygnus X-3 with GRS 1915+105 and XTE J1550$-$564 (Szostek et al. 2008; Hjalmarsdotter et al. 2009). Also, a model-independent study by Vrtilek and Boroson (2013) showed that Cygnus X-3 shares space between GRS 1915+105 -like black hole systems and pulsars in the color-color-intensity volume. However, the hallmark of pulsars – regular X-ray pulsations – have not been observed from Cygnus X-3 and also the X-ray spectra of pulsars are rather different to those observed from Cygnus X-3. Thus, the most likely compact object is a low-mass black hole. Interestingly, 2–5 $M_\odot$ compact objects are not found to abound in the Universe (Belczynski et al. 2012, and references therein) and this compact object mass region is often dubbed the “mass gap”. If indeed the low-mass black hole nature is confirmed in the future this adds yet another unique aspect to Cygnus X-3.

A note should be made about possible neutrino emission from Cygnus X-3. It has been estimated by Distefano et al. (2002) that Cygnus X-3 should be the brightest neutrino emitter in the Galaxy, in the context of a hadronic jet, where protons colliding with synchrotron photons produce neutrinos. In this scenario the neutrino flux would precede the γ-ray flares, and thus the above-mentioned order of events in the major flaring episode becomes important. If a neutrino flux is observed from Cygnus X-3, it certainly would help assessing the composition of the jet and help narrowing down the birth of the jet. However, neutrinos have not been observed so far from Cygnus X-3 (IceCube Collaboration et al. 2013). On the other hand, this gives more credibility to the leptonic composition of the jet.

5.2 Concluding remarks

To conclude, it is evident that the jet plays a major role in the nature of Cygnus X-3. By implementing a careful analysis of the X-ray data in the spectral, timing and spectrotiming domains with supporting observations across the electromagnetic spectrum, it has been demonstrated in this thesis that new features can be found even in a source studied for such a long time. These features include the softest X-ray state, i.e. the hypersoft state, when the source exhibits quenching in the radio and hard X-rays. When Cygnus X-3 descends into the hypersoft state γ-ray flares are observed possibly indicating the birth of the jet. Likewise when Cygnus X-3 ascends from the hypersoft state γ-ray flares are observed again followed by a major radio flare, the jet becoming visible in the radio images, and the recovery of the hard X-rays. What remains to be solved is the overall model to explain this behavior: the order of these events which appear to occur in the inverse sense when compared to other microquasars/XRBs, the nature of the hypersoft state and the mechanisms of the radio and hard X-ray quenching and the mechanism producing the γ-ray emission. In this thesis it has been debated that the link between the jet and the hard X-rays is in the form of Comptonization: the jet producing the population of hot electrons Compton upscatters the seed photons thereby explaining the radio/hard X-ray correlation. By utilizing PCA to study the time evolution of X-ray spectra it has been shown in this thesis that the seed photon population can arise from two distinct populations, one colder (presumably from the accretion disk) and one hotter (presumably from a hot, thermal plasma around the compact object). The advantages of ruling out spectral models with this method should be enticing to the X-ray community. Still more effects caused by the jet could be the sporadic detections of low-frequency QPOs coinciding with the aftermath of the jet ejection. While the origin of these QPOs remains to be investigated it is interesting to note that they occur in the orbital phase when we should observe the jet. Thus, it might be possible to study the connection between the jet and the interstellar medium close to Cygnus X-3 with the aid of the underlying X-ray emission. While Cygnus X-3 is a very complex source it is also very rewarding in that it produces one interesting phenomenon after the other. Although a complete model of the source is yet to be seen, hopefully this work has moved us a notch towards complete understanding of this enigmatic microquasar.

Bibliography

J. Aleksić, L. A. Antonelli, P. Antoranz, M. Backes, C. Baixeras, J. A. Barrio, D. Bastieri, J. Becerra González, W. Bednarek, A. Berdyugin, K. Berger, E. Bernardini, A. Biland, O. Blanch, R. K. Bock, A. Boller, G. Bonnoli, P. Bordas, D. Borla Tridon, V. Bosch-Ramon, D. Bose, I. Braun, T. Bretz, D. Britzger, M. Camara, E. Carmona, A. Carosi, P. Colin, J. L. Contreras, J. Cortina, M. T. Costado, S. Covino, F. Dazzi, A. De Angelis, E. De Cea del Pozo, B. De Lotto, M. De Maria, F. De Sabata, C. Delgado Mendez, M. Doert, A. Domínguez, D. Dominis Prester, D. Dorner, M. Doro, D. Elsaesser, M. Errando, D. Ferenc, M. V. Fonseca, L. Font, R. J. García López, M. Garczarczyk, M. Gaug, N. Godinovic, F. Göebel, D. Hadasch, A. Herrero, D. Hildebrand, D. Höhne-Mönch, J. Hose, D. Hrupec, C. C. Hsu, T. Jogler, S. Klepser, T. Krähenbühl, D. Kranich, A. La Barbera, A. Laille, E. Leonardo, E. Lindfors, S. Lombardi, F. Longo, M. López, E. Lorenz, P. Majumdar, G. Maneva, N. Mankuzhiyil, K. Mannheim, L. Maraschi, M. Mariotti, M. Martínez, D. Mazin, M. Meucci, J. M. Miranda, R. Mirzoyan, H. Miyamoto, J. Moldón, M. Moles, A. Moralejo, D. Nieto, K. Nilsson, J. Ninkovic, R. Orito, I. Oya, S. Paiano, R. Paoletti, J. M. Paredes, S. Partini, M. Pasanen, D. Pascoli, F. Pauss, R. G. Pegna, M. A. Perez-Torres, M. Persic, L. Peruzzo, F. Prada, E. Prandini, N. Puchades, I. Puljak, I. Reichardt, W. Rhode, M. Ribó, J. Rico, M. Rissi, S. Rügamer, A. Saggion, K. Saito, T. Y. Saito, M. Salvati, M. Sánchez-Conde, K. Satalecka, V. Scalzotto, V. Scapin, C. Schultz, T. Schweizer, M. Shayduk, S. N. Shore, A. Sierpowska-Bartosik, A. Sillanpää, J. Sitarek, D. Sobczynska, F. Spanier, S. Spiro, A. Stamerra, B. Steinke, J. C. Struebig, T. Suric, L. Takalo, F. Tavecchio, P. Temnikov, T. Terzic, D. Tescaro, M. Teshima, D. F. Torres, H. Vankov, R. M. Wagner, Q. Weitzel, V. Zabalza, F. Zandanel, R. Zanin, and MAGIC Collaboration. Magic Constraints on γ-ray Emission from Cygnus X-3. *ApJ*, 721:843–855, September 2010.

M. Axelsson, S. Larsson, and L. Hjalmarsdotter. The aperiodic broad-band X-ray variability of Cygnus X-3. *MNRAS*, 394:1544–1550, April 2009.

S. A. Balbus and J. F. Hawley. Instability, turbulence, and enhanced transport in accretion disks. *Reviews of Modern Physics*, 70:1–53, January 1998.

G. Barbiellini, G. Fedel, F. Liello, F. Longo, C. Pontoni, M. Prest, M. Tavani, and E. Vallazza. The AGILE silicon tracker: testbeam results of the prototype silicon detector. *Nuclear Instruments and Methods in Physics Research A*, 490: 146–158, September 2002.

K. Belczynski, G. Wiktorowicz, C. L. Fryer, D. E. Holz, and V. Kalogera. Missing black holes unveil the supernova explosion mechanism. *ApJ*, 757:91, September 2012.

T. Belloni, J. Homan, P. Casella, M. van der Klis, E. Nespoli, W. H. G. Lewin, J. M. Miller, and M. Méndez. The evolution of the timing properties of the black-hole transient GX 339-4 during its 2002/2003 outburst. *A&A*, 440:207–222, September 2005.

S. Benlloch, J. Wilms, R. Edelson, T. Yaqoob, and R. Staubert. Quasi-periodic oscillation in Seyfert galaxies: significance levels. The case of Markarian 766. *ApJ*, 562:L121–L124, December 2001.

P. R. Bevington and D. K. Robinson. *Data reduction and error analysis for the physical sciences*. McGraw-Hill, 1992.

C. L. Bhat, M. L. Sapru, and H. Razdan. Estimate from Gulmarg of PeV photon flux from Cygnus X-3 and its relevance. *ApJ*, 306:587–598, July 1986.

B. Binder, B. F. Williams, M. Eracleous, M. R. Garcia, S. F. Anderson, and T. J. Gaetz. A deep Chandra observation of the Wolf-Rayet + black hole binary NGC 300 X-1. *ApJ*, 742:128, December 2011.

R. D. Blandford. Accretion disc electrodynamics - A model for double radio sources. *MNRAS*, 176:465–481, September 1976.

R. D. Blandford and D. G. Payne. Hydromagnetic flows from accretion discs and the production of radio jets. *MNRAS*, 199:883–903, June 1982.

R. D. Blandford and R. L. Znajek. Electromagnetic extraction of energy from Kerr black holes. *MNRAS*, 179:433–456, May 1977.

A. Bulgarelli, M. Tavani, A. W. Chen, Y. Evangelista, M. Trifoglio, F. Gianotti, G. Piano, S. Sabatini, E. Striani, G. Pooley, S. Trushkin, N. A. Nizhelskij, M. McCollough, K. I. I. Koljonen, D. Hannikainen, A. Lähteenmäki, J. Tammi, N. Lavonen, D. Steeghs, A. Aboudan, A. Argan, G. Barbiellini, R. Campana, P. Caraveo, P. W. Cattaneo, V. Cocco, T. Contessi, E. Costa, F. D'Ammando, E. Del Monte, G. de Paris, G. Di Cocco, I. Donnarumma, M. Feroci, M. Fiorini, F. Fuschino, M. Galli, A. Giuliani, M. Giusti, C. Labanti, I. Lapshov, F. Lazzarotto, P. Lipari, F. Longo, M. Marisaldi, S. Mereghetti, E. Morelli, E. Moretti, A. Morselli, L. Pacciani, A. Pellizzoni, F. Perotti, P. Picozza, M. Pilia, M. Prest, G. Pucella, M. Rapisarda, A. Rappoldi, A. Rubini, P. Soffitta, A. Trois, E. Vallazza, S. Vercellone, V. Vittorini, A. Zambra, D. Zanello, P. Giommi, C. Pittori, F. Verrecchia, P. Santolamazza, F. Lucarelli, S. Colafrancesco, and L. Salotti. AGILE detection of Cygnus X-3 γ-ray active states during the period mid-2009/mid-2010. *A&A*, 538:A63, February 2012.

T. Bulik, K. Belczynski, and A. Prestwich. IC10 X-1/NGC300 X-1: the very immediate progenitors of BH-BH binaries. *ApJ*, 730:140, April 2011.

S. Carpano, A. M. T. Pollock, A. Prestwich, P. Crowther, J. Wilms, L. Yungelson, and M. Ehle. A 33 hour period for the Wolf-Rayet/black hole X-ray binary candidate NGC 300 X-1. *A&A*, 466:L17–L20, May 2007.

M. Choudhury, A. R. Rao, S. V. Vadawale, A. K. Jain, and N. S. Singh. Binary corrected X-ray light curve of Cygnus X-3: implications for the timing properties of the compact binary system. *A&A*, 420:665–671, June 2004.

S. Corbel, G. Dubus, J. A. Tomsick, A. Szostek, R. H. D. Corbet, J. C. A. Miller-Jones, J. L. Richards, G. Pooley, S. Trushkin, R. Dubois, A. B. Hill, M. Kerr, W. Max-Moerbeck, A. C. S. Readhead, A. Bodaghee, V. Tudose, D. Parent, J. Wilms, and K. Pottschmidt. A giant radio flare from Cygnus X-3 with associated γ-ray emission. *MNRAS*, 421:2947–2955, April 2012.

P. A. Crowther, R. Barnard, S. Carpano, J. S. Clark, V. S. Dhillon, and A. M. T. Pollock. NGC 300 X-1 is a Wolf-Rayet/black hole binary. *MNRAS*, 403:L41–L45, March 2010.

S. Danaher, D. J. Fegan, N. A. Porter, and T. C. Weekes. Gamma-ray observations of Cygnus X-3 at energies of 10 to the 12th eV. *Nat*, 289:568–569, February 1981.

G. Di Cocco, E. Caroli, E. Celesti, L. Foschini, F. Gianotti, C. Labanti, G. Malaguti, A. Mauri, E. Rossi, F. Schiavone, A. Spizzichino, J. B. Stephen, A. Traci, and M. Trifoglio. IBIS/PICsIT in-flight performances. *A&A*, 411: L189–L195, November 2003.

J. M. Dickey. A new distance to Cygnus X-3. *ApJ*, 273:L71–L73, October 1983.

C. Distefano, D. Guetta, E. Waxman, and A. Levinson. Neutrino flux predictions for known galactic microquasars. *ApJ*, 575:378–383, August 2002.

G. Dubus, B. Cerutti, and G. Henri. The relativistic jet of Cygnus X-3 in gamma-rays. *MNRAS*, 404:L55–L59, May 2010.

R. P. Fender, M. M. Hanson, and G. G. Pooley. Infrared spectroscopic variability of Cygnus X-3 in outburst and quiescence. *MNRAS*, 308:473–484, September 1999.

R. P. Fender, T. M. Belloni, and E. Gallo. Towards a unified model for black hole X-ray binary jets. *MNRAS*, 355:1105–1118, December 2004.

R. P. Fender, J. Homan, and T. M. Belloni. Jets from black hole X-ray binaries: testing, refining and extending empirical models for the coupling to X-rays. *MNRAS*, 396:1370–1382, July 2009.

Fermi LAT Collaboration, A. A. Abdo, M. Ackermann, M. Ajello, M. Axelsson, L. Baldini, J. Ballet, G. Barbiellini, D. Bastieri, B. M. Baughman, K. Bechtol, R. Bellazzini, B. Berenji, R. D. Blandford, E. D. Bloom, E. Bonamente, A. W. Borgland, A. Brez, M. Brigida, P. Bruel, T. H. Burnett, S. Buson, G. A. Caliandro, R. A. Cameron, P. A. Caraveo, J. M. Casandjian, C. Cecchi, Ö. Çelik, S. Chaty, C. C. Cheung, J. Chiang, S. Ciprini, R. Claus, J. Cohen-Tanugi, L. R. Cominsky, J. Conrad, S. Corbel, R. Corbet, C. D. Dermer, F. de Palma, S. W. Digel, E. do Couto e Silva, P. S. Drell, R. Dubois, G. Dubus, D. Dumora, C. Farnier, C. Favuzzi, S. J. Fegan, W. B. Focke, P. Fortin, M. Frailis, P. Fusco, F. Gargano, N. Gehrels, S. Germani, G. Giavitto, B. Giebels, N. Giglietto, F. Giordano, T. Glanzman, G. Godfrey, I. A. Grenier, M.-H. Grondin, J. E. Grove, L. Guillemot, S. Guiriec, Y. Hanabata, A. K. Harding, M. Hayashida, E. Hays, A. B. Hill, L. Hjalmarsdotter, D. Horan, R. E. Hughes, M. S. Jackson, G. Jóhannesson, A. S. Johnson, T. J. Johnson, W. N. Johnson, T. Kamae, H. Katagiri, N. Kawai, M. Kerr, J. Knödlseder, M. L. Kocian, E. Koerding, M. Kuss, J. Lande, J. Latronico, M. Lemoine-Goumard, F. Longo, F. Loparco, B. Lott, M. N. Lovellette, P. Lubrano, G. M. Madejski, A. Makeev, L. Marchand,

M. Marelli, W. Max-Moerbeck, M. N. Mazziotta, N. McColl, J. E. McEnery, C. Meurer, P. F. Michelson, S. Migliari, W. Mitthumsiri, T. Mizuno, C. Monte, M. E. Monzani, A. Morselli, I. V. Moskalenko, S. Murgia, P. L. Nolan, J. P. Norris, E. Nuss, T. Ohsugi, N. Omodei, R. A. Ong, J. F. Ormes, D. Paneque, D. Parent, V. Pelassa, M. Pepe, M. Pesce-Rollins, F. Piron, G. Pooley, T. A. Porter, K. Pottschmidt, S. Rainò, R. Rando, P. S. Ray, M. Razzano, N. Rea, A. Readhead, A. Reimer, O. Reimer, J. L. Richards, L. S. Rochester, J. Rodriguez, A. Y. Rodriguez, R. W. Romani, F. Ryde, H. F.-W. Sadrozinski, A. Sander, P. M. Saz Parkinson, C. Sgrò, E. J. Siskind, D. A. Smith, P. D. Smith, P. Spinelli, J.-L. Starck, M. Stevenson, M. S. Strickman, D. J. Suson, H. Takahashi, T. Tanaka, J. B. Thayer, D. J. Thompson, L. Tibaldo, J. A. Tomsick, D. F. Torres, G. Tosti, A. Tramacere, Y. Uchiyama, T. L. Usher, V. Vasileiou, N. Vilchez, V. Vitale, A. P. Waite, P. Wang, J. Wilms, B. L. Winer, K. W. Wood, T. Ylinen, and M. Ziegler. Modulated high-energy gamma-ray emission from the microquasar Cygnus X-3. *Science*, 326:1512–1516, December 2009.

M. Feroci, E. Costa, P. Soffitta, E. Del Monte, G. di Persio, I. Donnarumma, Y. Evangelista, M. Frutti, I. Lapshov, F. Lazzarotto, M. Mastropietro, E. Morelli, L. Pacciani, G. Porrovecchio, M. Rapisarda, A. Rubini, M. Tavani, and A. Argan. SuperAGILE: the hard X-ray imager for the AGILE space mission. *Nuclear Instruments and Methods in Physics Research A*, 581:728–754, November 2007.

N. Gehrels, G. Chincarini, P. Giommi, K. O. Mason, J. A. Nousek, A. A. Wells, N. E. White, S. D. Barthelmy, D. N. Burrows, L. R. Cominsky, K. C. Hurley, F. E. Marshall, P. Mészáros, P. W. A. Roming, L. Angelini, L. M. Barbier, T. Belloni, S. Campana, P. A. Caraveo, M. M. Chester, O. Citterio, T. L. Cline, M. S. Cropper, J. R. Cummings, A. J. Dean, E. D. Feigelson, E. E. Fenimore, D. A. Frail, A. S. Fruchter, G. P. Garmire, K. Gendreau, G. Ghisellini, J. Greiner, J. E. Hill, S. D. Hunsberger, H. A. Krimm, S. R. Kulkarni, P. Kumar, F. Lebrun, N. M. Lloyd-Ronning, C. B. Markwardt, B. J. Mattson, R. F. Mushotzky, J. P. Norris, J. Osborne, B. Paczynski, D. M. Palmer, H.-S. Park, A. M. Parsons, J. Paul, M. J. Rees, C. S. Reynolds, J. E. Rhoads, T. P. Sasseen, B. E. Schaefer, A. T. Short, A. P. Smale, I. A. Smith, L. Stella, G. Tagliaferri, T. Takahashi, M. Tashiro, L. K. Townsley, J. Tueller, M. J. L. Turner, M. Vietri, W. Voges, M. J. Ward, R. Willingale, F. M. Zerbi, and W. W. Zhang. The Swift Gamma-ray Burst Mission. *ApJ*, 611:1005–1020, August 2004.

R. Giacconi, P. Gorenstein, H. Gursky, and J. R. Waters. An X-ray survey of the Cygnus region. *ApJ*, 148:L119–L127, June 1967.

W. Hermsen, J. B. G. M. Bloemen, F. A. Jansen, K. Bennett, R. Buccheri, A. Mastichiadis, H. A. Mayer-Hasselwander, A. W. Strong, M. E. Oezel, and A. M. T. Pollock. High-energy gamma-ray and hard X-ray observations of Cyg X-3. *A&A*, 175:141–150, March 1987.

L. Hjalmarsdotter, A. A. Zdziarski, A. Szostek, and D. C. Hannikainen. Spectral variability in Cygnus X-3. *MNRAS*, 392:251–263, January 2009.

IceCube Collaboration, R. Abbasi, Y. Abdou, M. Ackermann, J. Adams, J. A. Aguilar, M. Ahlers, D. Altmann, K. Andeen, J. Auffenberg, X. Bai, M. Baker, S. W. Barwick, V. Baum, R. Bay, K. Beattie, J. J. Beatty, S. Bechet, J. Becker Tjus, K.-H. Becker, M. Bell, M. L. Benabderrahmane, S. BenZvi, J. Berdermann, P. Berghaus, D. Berley, E. Bernardini, D. Bertrand, D. Z. Besson,

D. Bindig, M. Bissok, E. Blaufuss, J. Blumenthal, D. J. Boersma, C. Bohm, D. Bose, S. Böser, O. Botner, L. Brayeur, A. M. Brown, R. Bruijn, J. Brunner, S. Buitink, M. Carson, J. Casey, M. Casier, D. Chirkin, B. Christy, F. Clevermann, S. Cohen, D. F. Cowen, A. H. Cruz Silva, M. Danninger, J. Daughhetee, J. C. Davis, C. De Clercq, F. Descamps, P. Desiati, G. de Vries-Uiterweerd, T. DeYoung, J. C. Díaz-Vélez, J. Dreyer, J. P. Dumm, M. Dunkman, R. Eagan, J. Eisch, R. W. Ellsworth, O. Engdegård, S. Euler, P. A. Evenson, O. Fadiran, A. R. Fazely, A. Fedynitch, J. Feintzeig, T. Feusels, K. Filimonov, C. Finley, T. Fischer-Wasels, S. Flis, A. Franckowiak, R. Franke, K. Frantzen, T. Fuchs, T. K. Gaisser, J. Gallagher, L. Gerhardt, L. Gladstone, T. Glüsenkamp, A. Goldschmidt, J. A. Goodman, D. Góra, D. Grant, A. Groß, S. Grullon, M. Gurtner, C. Ha, A. Haj Ismail, A. Hallgren, F. Halzen, K. Hanson, D. Heereman, P. Heimann, D. Heinen, K. Helbing, R. Hellauer, S. Hickford, G. C. Hill, K. D. Hoffman, R. Hoffmann, A. Homeier, K. Hoshina, W. Huelsnitz, P. O. Hulth, K. Hultqvist, S. Hussain, A. Ishihara, E. Jacobi, J. Jacobsen, G. S. Japaridze, O. Jlelati, A. Kappes, T. Karg, A. Karle, J. Kiryluk, F. Kislat, J. Kläs, S. R. Klein, J.-H. Köhne, G. Kohnen, H. Kolanoski, L. Köpke, C. Kopper, S. Kopper, D. J. Koskinen, M. Kowalski, M. Krasberg, G. Kroll, J. Kunnen, N. Kurahashi, T. Kuwabara, M. Labare, K. Laihem, H. Landsman, M. J. Larson, R. Lauer, M. Lesiak-Bzdak, J. Lünemann, J. Madsen, R. Maruyama, K. Mase, H. S. Matis, F. McNally, K. Meagher, M. Merck, P. Mészáros, T. Meures, S. Miarecki, E. Middell, N. Milke, J. Miller, L. Mohrmann, T. Montaruli, R. Morse, S. M. Movit, R. Nahnhauer, U. Naumann, S. C. Nowicki, D. R. Nygren, A. Obertacke, S. Odrowski, A. Olivas, M. Olivo, A. O'Murchadha, S. Panknin, L. Paul, C. Pepper, J. A. Pérez de los Heros, D. Pieloth, N. Pirk, J. Posselt, P. B. Price, G. T. Przybylski, L. Rädel, K. Rawlins, P. Redl, E. Resconi, W. Rhode, M. Ribordy, M. Richman, B. Riedel, J. P. Rodrigues, F. Rothmaier, C. Rott, T. Ruhe, B. Ruzybayev, D. Ryckbosch, S. M. Saba, T. Salameh, H.-G. Sander, M. Santander, S. Sarkar, K. Schatto, M. Scheel, F. Scheriau, T. Schmidt, M. Schmitz, S. Schoenen, S. Schöneberg, L. Schönherr, A. Schönwald, A. Schukraft, L. Schulte, O. Schulz, D. Seckel, S. H. Seo, Y. Sestayo, S. Seunarine, M. W. E. Smith, M. Soiron, D. Soldin, G. M. Spiczak, C. Spiering, M. Stamatikos, T. Stanev, A. Stasik, T. Stezelberger, R. G. Stokstad, A. Stößl, E. A. Strahler, R. Ström, G. W. Sullivan, H. Taavola, I. Taboada, A. Tamburro, S. Ter-Antonyan, S. Tilav, P. A. Toale, S. Toscano, M. Usner, D. van der Drift, N. van Eijndhoven, A. Van Overloop, J. van Santen, M. Vehring, M. Voge, C. Walck, T. Waldenmaier, M. Wallraff, M. Walter, R. Wasserman, Ch. Weaver, C. Wendt, S. Westerhoff, N. Whitehorn, K. Wiebe, C. H. Wiebusch, D. R. Williams, H. Wissing, M. Wolf, T. R. Wood, K. Woschnagg, C. Xu, D. L. Xu, X. W. Xu, J. P. Yanez, G. Yodh, S. Yoshida, P. Zarzhitsky, J. Ziemann, A. Zilles, and M. Zoll. Searches for high-energy neutrino emission in the Galaxy with the combined ICECUBE-AMANDA detector. *ApJ*, 763:33, January 2013.

S. Ichimaru. Bimodal behavior of accretion disks - Theory and application to Cygnus X-1 transitions. *ApJ*, 214:840–855, June 1977.

K. Jahoda, J. H. Swank, A. B. Giles, M. J. Stark, T. Strohmayer, W. Zhang, and E. H. Morgan. In-orbit performance and calibration of the Rossi X-ray Timing Explorer (RXTE) Proportional Counter Array (PCA). In O. H. Siegmund and M. A. Gummin, editors, *Society of Photo-Optical Instrumentation Engineers (SPIE) Conference Series*, volume 2808 of *Society of Photo-Optical Instrumentation Engineers (SPIE) Conference Series*, pages 59–70, October 1996.

R. C. Lamb, C. P. Godfrey, W. A. Wheaton, and T. Tumer. Cygnus X-3 observed at photon energies above 500 GeV. *Nat*, 296:543–544, April 1982.

F. Lebrun, J. P. Leray, P. Lavocat, J. Crétolle, M. Arquès, C. Blondel, C. Bonnin, A. Bouère, C. Cara, T. Chaleil, F. Daly, F. Desages, H. Dzitko, B. Horeau, P. Laurent, O. Limousin, F. Mathy, V. Mauguen, F. Meignier, F. Molinié, E. Poindron, M. Rouger, A. Sauvageon, and T. Tourrette. ISGRI: the INTEGRAL Soft Gamma-Ray Imager. *A&A*, 411:L141–L148, November 2003.

A. M. Levine, H. Bradt, W. Cui, J. G. Jernigan, E. H. Morgan, R. Remillard, R. E. Shirey, and D. A. Smith. First results from the All-Sky Monitor on the Rossi X-ray Timing Explorer. *ApJ*, 469:L33–L36, September 1996.

E. J. Lindfors, M. Türler, D. C. Hannikainen, G. Pooley, J. Tammi, S. A. Trushkin, and E. Valtaoja. Synchrotron flaring behaviour of Cygnus X-3 during the February-March 1994 and September 2001 outbursts. *A&A*, 473:923–929, October 2007.

Z. Ling, S. N. Zhang, and S. Tang. Determining the distance of Cyg X-3 with its X-ray dust scattering halo. *ApJ*, 695:1111–1120, April 2009.

Q. Z. Liu, J. van Paradijs, and E. P. J. van den Heuvel. Catalogue of high-mass X-ray binaries in the Galaxy (4th edition). *A&A*, 455:1165–1168, September 2006.

Q. Z. Liu, J. van Paradijs, and E. P. J. van den Heuvel. A catalogue of low-mass X-ray binaries in the Galaxy, LMC, and SMC (Fourth edition). *A&A*, 469:807–810, July 2007.

D. Lommen, L. Yungelson, E. van den Heuvel, G. Nelemans, and S. Portegies Zwart. Cygnus X-3 and the problem of the missing Wolf-Rayet X-ray binaries. *A&A*, 443:231–241, November 2005.

M. S. Longair. *High Energy Astrophysics*. Cambridge University Press, 2011.

R. V. E. Lovelace. Dynamo model of double radio sources. *Nat*, 262:649–652, August 1976.

N. Lund, C. Budtz-Jørgensen, N. J. Westergaard, S. Brandt, I. L. Rasmussen, A. Hornstrup, C. A. Oxborrow, J. Chenevez, P. A. Jensen, S. Laursen, K. H. Andersen, P. B. Mogensen, I. Rasmussen, K. Omø, S. M. Pedersen, J. Polny, H. Andersson, T. Andersson, V. Kämäräinen, O. Vilhu, J. Huovelin, S. Maisala, M. Morawski, G. Juchnikowski, E. Costa, M. Feroci, A. Rubini, M. Rapisarda, E. Morelli, V. Carassiti, F. Frontera, C. Pelliciari, G. Loffredo, S. Martínez Núñez, V. Reglero, T. Velasco, S. Larsson, R. Svensson, A. A. Zdziarski, A. Castro-Tirado, P. Attina, M. Goria, G. Giulianelli, F. Cordero, M. Rezazad, M. Schmidt, R. Carli, C. Gomez, P. L. Jensen, G. Sarri, A. Tiemon, A. Orr, R. Much, P. Kretschmar, and H. W. Schnopper. JEM-X: the X-ray monitor aboard INTEGRAL. *A&A*, 411:L231–L238, November 2003.

J. M. Mas-Hesse, A. Giménez, J. L. Culhane, C. Jamar, B. McBreen, J. Torra, R. Hudec, J. Fabregat, E. Meurs, J. P. Swings, M. A. Alcacera, A. Balado, R. Beiztegui, T. Belenguer, L. Bradley, M. D. Caballero, P. Cabo, J. M. Defise, E. Díaz, A. Domingo, F. Figueras, I. Figueroa, L. Hanlon, F. Hroch, V. Hudcova, T. García, B. Jordan, C. Jordi, P. Kretschmar, C. Laviada, M. March, E. Martín, E. Mazy, M. Menéndez, J. M. Mi, E. de Miguel, T. Muñoz, K. Nolan, R. Olmedo,

J. Y. Plesseria, J. Polcar, M. Reina, E. Renotte, P. Rochus, A. Sánchez, J. C. San Martín, A. Smith, J. Soldan, P. Thomas, V. Timón, and D. Walton. OMC: an Optical Monitoring Camera for INTEGRAL. Instrument description and performance. *A&A*, 411:L261–L268, November 2003.

K. O. Mason, F. A. Cordova, and N. E. White. Simultaneous X-ray and infrared observations of Cygnus X-3. *ApJ*, 309:700–706, October 1986.

J. E. McClintock and R. A. Remillard. Black hole binaries. In W. H. G. Lewin and M. van der Klis, editors, *Compact stellar X-ray sources*, pages 157–213. April 2006.

M. L. McCollough, C. R. Robinson, S. N. Zhang, B. A. Harmon, R. M. Hjellming, E. B. Waltman, R. S. Foster, F. D. Ghigo, M. S. Briggs, G. N. Pendleton, and K. J. Johnston. Discovery of correlated behavior between the hard X-ray and the radio bands in Cygnus X-3. *ApJ*, 517:951–955, June 1999.

M. L. McConnell, A. A. Zdziarski, K. Bennett, H. Bloemen, W. Collmar, W. Hermsen, L. Kuiper, W. Paciesas, B. F. Phlips, J. Poutanen, J. M. Ryan, V. Schönfelder, H. Steinle, and A. W. Strong. The soft gamma-ray spectral variability of Cygnus X-1. *ApJ*, 572:984–995, June 2002.

S. Migliari, R. P. Fender, M. Rupen, P. G. Jonker, M. Klein-Wolt, R. M. Hjellming, and M. van der Klis. Disc-jet coupling in an atoll-type neutron star X-ray binary: 4U 1728-34 (GX 354-0). *MNRAS*, 342:L67–L71, July 2003.

J. C. A. Miller-Jones, K. M. Blundell, M. P. Rupen, A. J. Mioduszewski, P. Duffy, and A. J. Beasley. Time-sequenced multi-radio frequency observations of Cygnus X-3 in flare. *ApJ*, 600:368–389, January 2004.

J. C. A. Miller-Jones, C. M. Sakari, V. Dhawan, V. Tudose, R. P. Fender, Z. Paragi, and M. Garrett. The proper motion and changing jet morphology of Cygnus X-3. In Conway J. E., editor, *The 8th International e-VLBI Workshop*, volume EXPReS09 of *Proceedings of Science (PoS)*, page 17, June 2009.

T. Mineo, E. Massaro, A. D'Ai, F. Massa, M. Feroci, G. Ventura, P. Casella, C. Ferrigno, and T. Belloni. The complex behaviour of the microquasar GRS 1915+105 in the ρ class observed with BeppoSAX. II. Time-resolved spectral analysis. *A&A*, 537:A18, January 2012.

A. J. Mioduszewski, M. P. Rupen, R. M. Hjellming, G. G. Pooley, and E. B. Waltman. A one-sided highly relativistic jet from Cygnus X-3. *ApJ*, 553:766–775, June 2001.

I. F. Mirabel and L. F. Rodríguez. A superluminal source in the Galaxy. *Nat*, 371: 46–48, September 1994.

M. Mori, D. L. Bertsch, B. L. Dingus, J. A. Esposito, C. E. Fichtel, S. D. Hunter, G. Kanbach, D. A. Kniffen, Y. C. Lin, J. R. Mattox, H. A. Mayer-Hasselwander, P. F. Michelson, C. von Montigny, R. Mukherjee, P. L. Nolan, P. V. Ramanamurthy, E. Schneid, P. Sreekumar, and D. J. Thompson. Cygnus X-3 and EGRET Gamma-Ray Observations. *ApJ*, 476:842, February 1997.

R. Narayan and I. Yi. Advection-dominated accretion: a self-similar solution. *ApJ*, 428:L13–L16, June 1994.

M. A. Nowak. Toward a Unified View of Black-Hole High-Energy States. *PASP*, 107:1207–1214, December 1995.

K. S. O'Flaherty, M. F. Cawley, D. J. Fegan, R. C. Lamb, M. J. Lang, D. A. Lewis, M. Punch, P. T. Reynolds, G. Vacanti, and T. C. Weekes. A search for TeV emission from Cygnus X-3. *ApJ*, 396:674–678, September 1992.

D. R. Parsignault, H. Gursky, E. M. Kellogg, T. Matilsky, S. Murray, E. Schreier, H. Tananbaum, R. Giacconi, and A. C. Brinkman. Observations of Cygnus X-3 by Uhuru. *Nature Physical Science*, 239:123–125, October 1972.

G. Piano, M. Tavani, V. Vittorini, A. Trois, A. Giuliani, A. Bulgarelli, Y. Evangelista, P. Coppi, E. Del Monte, S. Sabatini, E. Striani, I. Donnarumma, D. Hannikainen, K. I. I. Koljonen, M. McCollough, G. Pooley, S. Trushkin, R. Zanin, G. Barbiellini, M. Cardillo, P. W. Cattaneo, A. W. Chen, S. Colafrancesco, M. Feroci, F. Fuschino, M. Giusti, F. Longo, A. Morselli, A. Pellizzoni, C. Pittori, G. Pucella, M. Rapisarda, A. Rappoldi, P. Soffitta, M. Trifoglio, S. Vercellone, and F. Verrecchia. The AGILE monitoring of Cygnus X-3: transient gamma-ray emission and spectral constraints. *A&A*, 545:A110, September 2012.

P. Predehl and J. H. M. M. Schmitt. X-raying the interstellar medium: ROSAT observations of dust scattering halos. *A&A*, 293:889–905, January 1995.

P. Predehl, V. Burwitz, F. Paerels, and J. Trümper. Chandra measurement of the geometrical distance to Cyg X-3 using its X-ray scattering halo. *A&A*, 357: L25–L28, May 2000.

P. Predehl, V. Burwitz, E. Costantini, and J. Trümper. Geometrical distance measurement of Cyg X-3 using its X-ray scattering halo. In H. Inoue and H. Kunieda, editors, *New Century of X-ray Astronomy*, volume 251 of *Astronomical Society of the Pacific Conference Series*, pages 46–49, 2001.

M. Prest, G. Barbiellini, G. Bordignon, G. Fedel, F. Liello, F. Longo, C. Pontoni, and E. Vallazza. The AGILE silicon tracker: an innovative /γ-ray instrument for space. *Nuclear Instruments and Methods in Physics Research A*, 501:280–287, March 2003.

A. H. Prestwich, R. Kilgard, P. A. Crowther, S. Carpano, A. M. T. Pollock, A. Zezas, S. H. Saar, T. P. Roberts, and M. J. Ward. The orbital period of the Wolf-Rayet binary IC 10 X-1: dynamic evidence that the compact object is a black hole. *ApJ*, 669:L21–L24, November 2007.

B. Punsly and F. V. Coroniti. Ergosphere-driven winds. *ApJ*, 354:583–615, May 1990.

B. Rani, A. C. Gupta, U. C. Joshi, S. Ganesh, and P. J. Wiita. Quasi-periodic oscillations of $\sim$15 minutes in the optical light curve of the BL Lac S5 0716+714. *ApJ*, 719:L153–L157, August 2010.

A. R. Rao, P. C. Agrawal, and R. K. Manchanda. Hard X-ray observations of Cygnus X-3. *A&A*, 241:127–130, January 1991.

R. C. Reis, J. M. Miller, and A. C. Fabian. Thermal emission from the stellar-mass black hole binary XTE J1118+480 in the low/hard state. *MNRAS*, 395: L52–L56, May 2009.

G. E. Romero, D. F. Torres, M. M. Kaufman Bernadó, and I. F. Mirabel. Hadronic gamma-ray emission from windy microquasars. *A&A*, 410:L1–L4, October 2003.

R. E. Rothschild, P. R. Blanco, D. E. Gruber, W. A. Heindl, D. R. MacDonald, D. C. Marsden, M. R. Pelling, L. R. Wayne, and P. L. Hink. In-flight performance of the High-Energy X-ray Timing Experiment on the Rossi X-ray Timing Explorer. *ApJ*, 496:538–549, March 1998.

A. Rushton, J. C. A. Miller-Jones, R. Campana, Y. Evangelista, Z. Paragi, T. J. Maccarone, G. G. Pooley, V. Tudose, R. P. Fender, R. E. Spencer, and V. Dhawan. A weak compact jet in a soft state of Cygnus X-1. *MNRAS*, 419: 3194–3199, February 2012.

G. B. Rybicki and A. P. Lightman. *Radiative processes in astrophysics*. Wiley-Interscience, 1979.

M. Samorski and W. Stamm. Detection of 2×10^{15} to 2×10^{16} eV gamma-rays from Cygnus X-3. *ApJ*, 268:L17–L21, May 1983.

E. Seifina and L. Titarchuk. On the nature of the compact object in SS 433: observational evidence of X-ray photon index saturation. *ApJ*, 722:586–604, October 2010.

N. I. Shakura and R. A. Sunyaev. Black holes in binary systems. Observational appearance. *A&A*, 24:337–355, 1973.

J. M. Silverman and A. V. Filippenko. On IC 10 X-1, the most massive known stellar-mass black hole. *ApJ*, 678:L17–L20, May 2008.

A. Szostek and A. A. Zdziarski. Effects of the stellar wind on X-ray spectra of Cygnus X-3. *MNRAS*, 386:593–607, May 2008.

A. Szostek, A. A. Zdziarski, and P. Lachowicz. RXTE observations of Cygnus X-3. In P. Kaaret, F. K. Lamb, and J. H. Swank, editors, *X-ray Timing 2003: Rossi and Beyond*, volume 714 of *American Institute of Physics Conference Series*, pages 113–115, July 2004.

A. Szostek, A. A. Zdziarski, and M. L. McCollough. A classification of the X-ray and radio states of Cyg X-3 and their long-term correlations. *MNRAS*, 388: 1001–1010, August 2008.

H. Tananbaum, H. Gursky, E. Kellogg, R. Giacconi, and C. Jones. Observation of a Correlated X-Ray Transition in Cygnus X-1. *ApJ*, 177:L5–L10, October 1972.

S. P. Tigelaar, R. P. Fender, R. P. J. Tilanus, E. Gallo, and G. G. Pooley. Quenched millimetre emission from Cygnus X-1 in a soft X-ray state. *MNRAS*, 352:1015–1018, August 2004.

J. Timmer and M. Koenig. On generating power law noise. *A&A*, 300:707–710, August 1995.

L. Titarchuk and E. Seifina. Discovery of photon index saturation in the black hole binary GRS 1915+105. *ApJ*, 706:1463–1483, December 2009.

J. A. Tomsick, K. Yamaoka, S. Corbel, P. Kaaret, E. Kalemci, and S. Migliari. Truncation of the inner accretion disk around a black hole at low luminosity. *ApJ*, 707:L87–L91, December 2009.

S. A. Trushkin, N. N. Bursov, and N. A. Nizhelskij. Flaring variability of microquasars. In S. K. Chakrabarti and A. S. Majumdar, editors, *American Institute of Physics Conference Series*, volume 1053 of *American Institute of Physics Conference Series*, pages 219–224, October 2008.

V. Tudose, J. C. A. Miller-Jones, R. P. Fender, Z. Paragi, C. Sakari, A. Szostek, M. A. Garrett, V. Dhawan, A. Rushton, R. E. Spencer, and M. van der Klis. Probing the behaviour of the X-ray binary Cygnus X-3 with very long baseline radio interferometry. *MNRAS*, 401:890–900, January 2010.

P. Ubertini, F. Lebrun, G. Di Cocco, A. Bazzano, A. J. Bird, K. Broenstad, A. Goldwurm, G. La Rosa, C. Labanti, P. Laurent, I. F. Mirabel, E. M. Quadrini, B. Ramsey, V. Reglero, L. Sabau, B. Sacco, R. Staubert, L. Vigroux, M. C. Weisskopf, and A. A. Zdziarski. IBIS: the Imager on-Board INTEGRAL. *A&A*, 411: L131–L139, November 2003.

M. van der Klis. Rapid X-ray Variability. In W. H. G. Lewin and M. van der Klis, editors, *Compact stellar X-ray sources*, pages 39–112. Cambridge University Press, April 2006.

M. van der Klis. Similarities in neutron star and black hole accretion. *ApJS*, 92: 511–519, June 1994.

M. van der Klis and F. A. Jansen. Transient quasi-periodic oscillations in the X-ray flux of Cygnus X-3. *Nat*, 313:768–771, February 1985.

M. H. van Kerkwijk, P. A. Charles, T. R. Geballe, D. L. King, G. K. Miley, L. A. Molnar, E. P. J. van den Heuvel, M. van der Klis, and J. van Paradijs. Infrared helium emission lines from Cygnus X-3 suggesting a Wolf-Rayet star companion. *Nat*, 355:703–705, February 1992.

G. Vedrenne, J.-P. Roques, V. Schönfelder, P. Mandrou, G. G. Lichti, A. von Kienlin, B. Cordier, S. Schanne, J. Knödlseder, G. Skinner, P. Jean, F. Sanchez, P. Caraveo, B. Teegarden, P. von Ballmoos, L. Bouchet, P. Paul, J. Matteson, S. Boggs, C. Wunderer, P. Leleux, G. Weidenspointner, P. Durouchoux, R. Diehl, A. Strong, M. Cassé, M. A. Clair, and Y. André. SPI: the Spectrometer aboard INTEGRAL. *A&A*, 411:L63–L70, November 2003.

O. Vilhu and D. C. Hannikainen. Modeling the X-ray light curves of Cygnus X-3. Possible role of the jet. *A&A*, 550:A48, February 2013.

O. Vilhu, L. Hjalmarsdotter, A. A. Zdziarski, A. Paizis, M. L. McCollough, V. Beckmann, T. J.-L. Courvoisier, K. Ebisawa, P. Goldoni, P. Hakala, D. Hannikainen, P. Kretschmar, and N. J. Westergaard. First INTEGRAL observations of Cygnus X-3. *A&A*, 411:L405–L410, November 2003.

B. M. Vladimirsky, A. A. Stepanian, and V. P. Fomin. High-energy gamma-ray outburst in the direction of the X-ray source Cyg X-3. In *International Cosmic Ray Conference*, volume 1 of *International Cosmic Ray Conference*, pages 456–460, 1973.

S. D. Vrtilek and B. S. Boroson. Model independent means of categorizing X-ray binaries - I. Colour-colour-intensity diagrams. *MNRAS*, 428:3693–3714, February 2013.

E. B. Waltman, F. D. Ghigo, K. J. Johnston, R. S. Foster, R. L. Fiedler, and J. H. Spencer. The evolution of outbursts in Cygnus X-3 at 2.25 and 8.3 GHz. *AJ*, 110:290–299, July 1995.

E. B. Waltman, R. S. Foster, G. G. Pooley, R. P. Fender, and F. D. Ghigo. Quenched radio emission in Cygnus X-3. *Astronomical Journal*, 112:2690–2698, December 1996.

P. K. G. Williams, J. A. Tomsick, A. Bodaghee, G. C. Bower, G. G. Pooley, K. Pottschmidt, J. Rodriguez, J. Wilms, S. Migliari, and S. A. Trushkin. The 2010 May Flaring Episode of Cygnus X-3 in Radio, X-rays, and γ-rays. *ApJ*, 733:L20, June 2011.

R. Willingale, A. R. King, and K. A. Pounds. EXOSAT MEDA observations of Cygnus X-3. *MNRAS*, 215:295–314, July 1985.

A. A. Zdziarski, R. Misra, and M. Gierliński. Compton scattering as the explanation of the peculiar X-ray properties of Cyg X-3. *MNRAS*, 402:767–775, February 2010.

A. A. Zdziarski, G. K. Skinner, G. G. Pooley, and P. Lubiński. X-ray variability patterns and radio/X-ray correlations in Cyg X-1. *MNRAS*, 416:1324–1339, September 2011.

A. A. Zdziarski, C. Maitra, A. Frankowski, G. K. Skinner, and R. Misra. Energy-dependent orbital modulation of X-rays and constraints on emission of the jet in Cyg X-3. *MNRAS*, 426:1031–1042, October 2012a.

A. A. Zdziarski, M. Sikora, G. Dubus, F. Yuan, B. Cerutti, and A. Ogorzałek. The gamma-ray emitting region of the jet in Cyg X-3. *MNRAS*, 421:2956–2968, April 2012b.

A. A. Zdziarski, J. Mikołajewska, and K. Belczyński. Cyg X-3: a low-mass black hole or a neutron star. *MNRAS*, 429:L104–L108, February 2013.

J. T. L. Zwart, R. W. Barker, P. Biddulph, D. Bly, R. C. Boysen, A. R. Brown, C. Clementson, M. Crofts, T. L. Culverhouse, J. Czeres, R. J. Dace, M. L. Davies, R. D'Alessandro, P. Doherty, K. Duggan, J. A. Ely, M. Felvus, F. Feroz, W. Flynn, T. M. O. Franzen, J. Geisbüsch, R. Génova-Santos, K. J. B. Grainge, W. F. Grainger, D. Hammett, R. E. Hills, M. P. Hobson, C. M. Holler, N. Hurley-Walker, R. Jilley, M. E. Jones, T. Kaneko, R. Kneissl, K. Lancaster, A. N. Lasenby, P. J. Marshall, F. Newton, O. Norris, I. Northrop, D. M. Odell, G. Petencin, J. C. Pober, G. G. Pooley, M. W. Pospieszalski, V. Quy, C. Rodríguez-Gonzálvez, R. D. E. Saunders, A. M. M. Scaife, J. Schofield, P. F. Scott, C. Shaw, T. W. Shimwell, H. Smith, A. C. Taylor, D. J. Titterington, M. Velić, E. M. Waldram, S. West, B. A. Wood, G. Yassin, and AMI Consortium. The Arcminute Microkelvin Imager. *MNRAS*, 391:1545–1558, December 2008.

P. T. Życki, C. Done, and D. A. Smith. On the complex disc-corona interactions in the soft spectral states of soft X-ray transients. *MNRAS*, 326:1367–1380, October 2001.

Aalto-DD 129/2013

Extremely energetic radiation observed in the universe is attributed to the accretion of matter by compact objects: black holes and neutron stars. Microquasars, dubbed as such because of their similar phenomenological appearance to extragalactic quasars, are accreting compact objects with resolved, relativistic jets emanating from the central source. Cygnus X-3 is one of the most peculiar sources amongst microquasars. It is one of the most radio- and X-ray-luminous objects in our Galaxy, and thus a prime target for studying the emission mechanisms that arise during violent outbursts detected from the source throughout the electromagnetic spectrum.

This thesis consists of constructing a hardness-intensity diagram from X-ray data with simultaneous radio observations from Cygnus X-3, searching for low-frequency quasi-periodic oscillations and using principal component analysis to distinguish the variability of emission components during outbursts.

9 789526 052960

ISBN 978-952-60-5296-0
ISBN 978-952-60-5297-7 (pdf)
ISSN-L 1799-4934
ISSN 1799-4934
ISSN 1799-4942 (pdf)

Aalto University
School of Electrical Engineering
Department of Radio Science and Engineering
www.aalto.fi

BUSINESS +
ECONOMY

ART +
DESIGN +
ARCHITECTURE

SCIENCE +
TECHNOLOGY

CROSSOVER

DOCTORAL
DISSERTATIONS